frontiers | Frontiers in Marine Science

TYPE Original Research
PUBLISHED 22 October 2024
DOI 10.3389/fmars.2024.1476425

OPEN ACCESS

EDITED BY
Weimin Huang,
Memorial University of Newfoundland, Canada

REVIEWED BY
Inam Ullah,
Gachon University, Republic of Korea
Zhigang Cao,
Chinese Academy of Sciences (CAS), China

*CORRESPONDENCE
Alexander Gilerson
gilerson@ccny.cuny.edu

RECEIVED 05 August 2024
ACCEPTED 23 September 2024
PUBLISHED 22 October 2024

CITATION
Gilerson A, Malinowski M, Agagliate J, Herrera-Estrella E, Tzortziou M, Tomlinson MC, Meredith A, Stumpf RP, Ondrusek M, Jiang L and Wang M (2024) Development of VIIRS-OLCI chlorophyll-a product for the coastal estuaries.
Front. Mar. Sci. 11:1476425.
doi: 10.3389/fmars.2024.1476425

Development of VIIRS-OLCI chlorophyll-a product for the coastal estuaries

Alexander Gilerson[1]*, Mateusz Malinowski[1], Jacopo Agagliate[1], Eder Herrera-Estrella[1], Maria Tzortziou[2], Michelle C. Tomlinson[3], Andrew Meredith[4], Richard P. Stumpf[3], Michael Ondrusek[5], Lide Jiang[5,6] and Menghua Wang[5]

[1]Optical Remote Sensing Laboratory, The City College of New York, CUNY, New York, NY, United States, [2]The City College of New York, CUNY, New York, NY, United States, [3]National Centers for Coastal Ocean Science, NOAA, Silver Spring, MD, United States, [4]Consolidated Safety Services, Inc., Fairfax, VA, United States, [5]NOAA NESDIS Center for Satellite Applications and Research, College Park, MD, United States, [6]CIRA at Colorado State University, Fort Collins, CO, United States

Coastal waters require monitoring of chlorophyll-a concentration (Chl-a) in a wide range of Chl-a from a few mg/m^3 to hundreds of mg/m^3, which is of interest to the fisheries industry, evaluation of climate change effects, ecological modeling and detection of Harmful Algal Blooms (HABs). Monitoring can be carried out from the Visible Infrared Imaging Radiometer Suite (VIIRS) and Ocean and Land Colour Instrument (OLCI) Ocean Color (OC) satellite sensors, which are currently on orbit and are expected to be the main operational OC sensors at least for the next decade. A Neural Network (NN) algorithm, which uses VIIRS M3-M5 reflectance bands and an I1 imaging band, was developed to estimate Chl-a in the Chesapeake Bay, for the whole range of Chl-a from clear waters in the Lower Bay to extreme bloom conditions in the Upper Bay and the Potomac River, where Chl-a can be used for bloom detection. The NN algorithm demonstrated a significant improvement in the Chl-a retrieval capabilities in comparison with other algorithms, which utilize only reflectance bands. OLCI NIR/red 709/665 nm bands red edge 2010 algorithm denoted as RE10 was also explored with several atmospheric corrections from EUMETSAT, NOAA and NASA. Good consistency between the two types of algorithms is shown for the bloom conditions and the whole range of waters in the Chesapeake Bay (with RE10 switch to OC4 for lower Chl-a) and these algorithms are recommended for the combined VIIRS-OLCI product for the estimation of Chl-a and bloom monitoring. The algorithms were expanded to the waters in Long Island Sound, demonstrating good performance.

KEYWORDS

chlorophyll-a concentration, coastal waters, neural network, VIIRS, OLCI

1 Introduction

In estuaries and adjacent coastal waters, algal blooms are both a key water quality indicator and a potential hazard (Tango and Batiuk, 2016; Karlson et al., 2021). High biomass blooms have implications for reducing water clarity and are indicators of eutrophication in coastal systems (Bricker et al., 2008; Le et al., 2013). Reduced water clarity and depleted oxygen in bottom waters can have deleterious effects on essential fish habitats such as submerged aquatic vegetation in estuaries, leading to a shift from benthic to pelagic-dominated system productivity (Bricker et al., 2008). Harmful Algal Blooms (HABs), pertaining to a class of phytoplankton that often contain toxins, occur in various coastal areas and have a strong impact on fisheries, tourism, and recreation industries, requiring improved monitoring of HABs by environmental and health programs. HABs are often difficult to locate through routine monitoring programs because of their patchiness, physical circulation of the water, and vertical migration of algal particles. As a first approximation, typically, the concentration of chlorophyll-a (Chl-a) is considered as a proxy for the strength of the algal bloom, while bloom effects can vary depending on the type of algal species (IOCCG, 2021). Satellites can support the monitoring of HABs if they provide frequent coverage and retrieve Chl-a over a wide range of concentrations. Improved temporal resolution, which could be provided by using remote sensing products from multiple satellite sensors, can improve efforts of monitoring and forecasting HABs in coastal and estuarine waters. Data should come from multiple ocean color sensors to improve coverage during periods of cloud cover or sun glint (a problem especially in spring and summer), and to provide multiple views of blooms within a day.

Ocean color algorithms are based on remote sensing reflectance, R_{rs} spectra with Chl-a dominating R_{rs} spectra in the blue in clear waters. These algorithms often fail in optically complex coastal and estuarine waters where HABs occur, due to the high absorption of colored dissolved organic matter (CDOM) and scattering from sediments. Therefore, it is important to develop Chl-a algorithms that are minimally influenced by CDOM and/or high sediment concentrations. Efforts have been made to improve Chl-a retrievals from the Visible Infrared Imaging Radiometer Suite (VIIRS) sensors operated by National Oceanic and Atmospheric Administration (NOAA) and from Sentinel-3 Ocean and Land Colour Instrument (OLCI) sensors processed by NOAA in collaboration with the European Organization for the Exploitation of Meteorological Satellites (EUMETSAT) (Wang and Son, 2016; Mikelsons and Wang, 2019; Liu and Wang, 2022; Mikelsons et al., 2022; Wynne et al., 2022). Currently, there are three VIIRS sensors (on the SNPP, NOAA-20 and NOAA-21 platforms) and two OLCI sensors on the Sentinel-3A and 3B in space with 750 m and 300 m spatial resolution (at nadir), respectively. With additional launches of VIIRS planned, these two groups of sensors are expected to provide reliable and stable multi-spectral Ocean Color (OC) data for the next decade and beyond. The NASA Phytoplankton, Aerosol, Cloud, ocean Ecosystem (PACE) mission (Werdell et al., 2019), which was successfully launched in February 2024, has a main hyperspectral Ocean Color Instrument (OCI), but with a relatively coarse spatial resolution of 1.0 km (at nadir), which is not often sufficient for many coastal areas. The availability of consistent data in a wide range of Chl-a, with appropriate temporal resolution, will expand the number of applications and agencies, which utilize remote sensing data to complement the field data they use for decision-making regarding HABs. While the definition of HABs can be different for different water bodies, for this work we only consider high biomass blooms with Chl-a above 25-30 mg/m^3, which require the attention of coastal managers. This does not imply anything related to toxicity or deleterious effects to wildlife or public health and relies on *in situ* sampling to determine phytoplankton species.

Large uncertainties in remote sensing reflectance (R_{rs}) retrieval in blue bands remain a major problem for OC satellite sensors in coastal areas because of difficulties in atmospheric correction and low R_{rs} at this part of the spectrum (Ransibrahmanakul and Stumpf, 2006; IOCCG, 2019). In addition, due to the inability to see through clouds with OC sensors, daily imagery from current satellite sensors may be obscured. When monitoring blooms in coastal areas the combination of insufficient atmospheric correction in coastal and estuarine waters, and missing imagery due to clouds and sun glint, can often hinder the use of satellites in monitoring and forecasting efforts. Large uncertainties make an estimation of Chl-a concentration unreliable using standard OCx algorithms, which include the 443 nm band. A Neural Network (NN) Chl-a algorithm (Ioannou et al., 2014), which avoids blue bands at 412 and 443 nm for VIIRS demonstrated good performance in variable water areas (El-Habashi et al., 2016, 2017, 2019). Specifically, based on field measurements and matchups with satellite data, it has been shown that the NN Chl-a algorithm is valuable for the detection of *Karenia brevis* (KB) algal blooms near the West Florida coast (El-Habashi et al., 2016, 2017). The algorithm performs similarly to the standard OCx algorithms in the open ocean and coastal waters for Chl-a < 10 mg/m^3 (El-Habashi et al., 2019), but usually cannot detect accurately for Chl-a > 10-15 mg/m^3. A near-infrared (NIR)/red Chl-a algorithm applied to the bands available on MEdium Resolution Imaging Spectrometer (MERIS) and OLCI sensors performs well at Chl-a > 5 mg/m^3 in the field (Stumpf and Tyler, 1988; Gitelson, 1992; Moses et al., 2009; Gilerson et al., 2010; Smith et al., 2018; Neil et al., 2020). Unfortunately, applying the NIR/red algorithm to VIIRS is impossible, since it lacks a 709 nm band. A special AC has been developed by the NOAA's National Centers for Coastal Ocean Science (NCCOS) group for OLCI and has been applied to top-of-atmosphere reflectance corrected for molecular scattering (Wynne et al., 2018). Thus, an accurate estimation of high Chl-a values remains elusive from VIIRS and even from other multi-spectral sensors with a richer set of bands.

In addition to M1-M5 bands in the visible, VIIRS sensors have an imaging band I1 which integrates radiances from 600 to 680 nm, centered around 640 nm with an almost rectangular spectral transmission function. Utilization of this band on VIIRS opens additional possibilities. This 640 nm band covers R_{rs} features related to the increase of specific phytoplankton absorption from small values at 600 nm to high at 675 nm and thus can be sensitive to high Chl-a. This band as 638_ag (aggregated to 750 m spatial resolution as all M reflective bands) on SNPP VIIRS and as 642_ag on NOAA-20 was added to the images using the Multi-Sensor Level-1 to Level-2 (MSL12) data processing system (Wang and Jiang, 2018)

and distributedthrough the NOAA CoastWatch (https://coastwatch.noaa.gov/).

NN and Machine learning algorithms are based on the training of large datasets of synthetic, field, or satellite data and have recently been developed to estimate Chl-a and other water parameters on the global and regional scales (Hieronymi et al., 2017; Pahlevan et al., 2020; Liu and Wang, 2022; Werther et al., 2022; Cao et al., 2024). Their performance also depends on the applied atmospheric correction (Hieronymi et al., 2017).

The Chesapeake Bay and Long Island Sound (LIS) are large US estuaries on the US East Coast, where Chl-a needs to be monitored synoptically due to the often-occurring algal blooms and hypoxia events (Aurin et al., 2010; Wolny et al., 2020; Wynne et al., 2022). They are highly variable environments. Algal blooms are patchy and small-scale changes in Chl-a occur rapidly, making synoptic measurements essential to resolve phytoplankton biomass (Anderson and Taylor, 2001; Harding et al., 2005). While well-established monitoring programs, such as the Chesapeake Bay Program, Save the Sound, and state-lead monitoring provide routine monthly sampling at select stations, daily synoptic satellite Chl-a covering the entire estuary provide a better estimate of biomass and capture transient blooms, often missed by routine sampling.

Multiple studies characterized well water optical properties in these estuaries from field measurements and satellite observations (Stumpf and Pennock, 1989; Magnuson et al., 2004; Tzortziou et al., 2006; Aurin et al., 2010; Shi and Wang, 2013; Zheng et al., 2015; Turner et al., 2022; Menendez and Tzortziou, 2024), atmospheric correction algorithms have been assessed (Windle et al., 2022; Sherman et al., 2023; Cao and Tzortziou, 2024) and algorithms for the retrieval of Chl-a were developed (Gitelson et al., 2007; Le et al., 2013; Freitas and Dierssen, 2019; Sherman et al., 2023) for the specific sensors in these waters beyond standard OC3 and OC4 algorithms (O'Reilly et al., 1998, 2019).

The goal of this work is to extend the previously developed VIIRS NN-Chl-a algorithm for higher Chl-a by including the I1 imaging band data (600-680 nm) on VIIRS, investigate different processing schemes for the optimal use of the NIR/red (red edge) algorithm (Gilerson et al., 2010) on OLCI and develop a field validated combined OLCI-VIIRS products to improve detection and surveillance of algal blooms in complex estuarine waters such as the Chesapeake Bay and Long Island Sound. A more reliable estimation of Chl-a over the range seen along the U.S. East Coast is expected to enhance satellite coverage to improve ecological models, fisheries applications, and provide early and reliable detection of various blooms to support coastal managers in aiding aquaculture activities and protecting public health.

OLCI passes the US East Coast around 10 am EST and VIIRS around 1:30 pm EST. Data from several sensors increase coverage, however, the benefits are beyond simple statistics because bloom conditions can change in several hours with changes in tide conditions and biological processes. Multiple observations per day were the main incentive for the launch of GOCI sensors, and the development of geostationary GLIMR and Geo-XO sensors (Schaeffer et al., 2023). The product described in this paper creates a capability that would allow an approximation of the multi-scene capability offered by the geostationary satellites.

In Section 2, the bio-optical model is discussed, which is used for the generation of a large dataset for NN training and testing, different NN approaches are evaluated, and the development of the NN Chl-a algorithm for VIIRS based on M3-M5 reflectance bands and I1 imaging band is described. In Section 3, validation of the NN algorithm on field and satellite data is provided together with the comparison of VIIRS NN and OLCI RE10 algorithms for a broad range of conditions with different OLCI atmospheric correction processing schemes, and expansion of the NN-OLCI product to LIS, validation on field data. A discussion and conclusions are in Section 4.

2 Materials and methods

2.1 Field data

Field data, which were used in bio-optical modeling, comparisons of modeled and field Chl-a and other parameters, included data from several Chesapeake Bay cruises. A very comprehensive dataset was acquired by the CCNY-NOAA group in August 2013 at 43 stations, which included Chl-a, inherent optical properties (IOPs) and reflectance spectra. Attenuation and absorption of water and CDOM spectra were measured by the ac-s instrument; backscattering at 5 wavelengths was measured by the bb-9 instrument, both included in the WETLABS (Philomath, OR) package. At each station, upwelling radiance $L_u(\lambda,0^-)$ was measured using a fiber bundle placed just beneath the water surface and connected to a GER spectroradiometer (SpectraVista, NY). The downwelling radiance above the surface $L_d(\lambda,0+)$ was measured by pointing the same probe bundle onto a Spectralon plate and the downwelling irradiance was determined as $E_d(\lambda,0+) = A\cdot\pi\cdot L_d(\lambda,0+)$, where A = 0.99 is the reflectance factor of the Spectralon plate (Labsphere, NH), constant for the spectrum in the range of wavelengths from 400 to 800 nm. The underwater remote sensing reflectance R_{rs}- is then calculated as $L_u(\lambda,0^-)/E_d(\lambda,0^-)$ sr^{-1}, which was adjusted for the propagation through the water-air interface to calculate above surface R_{rs}. Chl-a from the samples that were collected during the field campaign were determined according to NASA protocol for fluorometric Chl-a determination (Ocean Optics Protocols, 2003).

Capturing the timing and location of a bloom is difficult, and often missing in routine monitoring datasets. An opportunistic sampling event occurred on May 18, 2021, during a high biomass (reaching up to 50 million cells/L) bloom of *Prorocentrum minimum*. R_{rs} and water samples for Chl-a were collected at 5 stations in the Upper Bay. Chl-a concentrations were measured in the range of 73–161 mg/m^3 and coincided in time with VIIRS and OLCI overpasses. Additional R_{rs} spectra and Chl-a were acquired in the Chesapeake Bay sporadically from 2014–2016, capturing a range of Chl-a of 9–48 mg/m^3. In all these measurements, R_{rs} were determined from below water HyperOCR depth profiles.

There was also a large dataset of NCCOS R_{rs} measurements but without corresponding Chl-a. All four R_{rs} datasets are shown below in Figure 1 in the discussion of the bio-optical model. Ranges of many parameters, necessary for the model and absorption spectra were

taken from the previous Chesapeake Bay cruises (Magnuson et al., 2004) and NASA bio-Optical Marine Algorithm Dataset (NOMAD) database (Werdell and Bailey, 2005). Finally, Chl-a data from the Chesapeake Bay program (https://www.chesapeakebay.net/) at multiple stations were used for the validation of the satellite and *in-situ* data, where most of Chl-a fell below 20 mg/m^3.

Concurrent water samples to extract Chl-a and hyperspectral R_{rs} were collected throughout LIS in 2018–2022 in collaboration with the Connecticut Department of Environmental Protection (CTDEEP) (Turner et al., 2022; Sherman et al., 2023). Additional data were collected from small boats. Hyperspectral R_{rs} were measured using a HR512-I spectroradiometer (SpectraVista, NY).

2.2 Satellite data and processing schemes

2.2.1 VIIRS data

The Level-2 science-quality data for SNPP VIIRS and near-real-time (NRT) for NOAA-20 VIIRS with the MSL12 processing were obtained from the NOAA CoastWatch site, featuring a pixel resolution of 750 meters at the nadir. This dataset included normalized water-leaving radiance spectra $nL_w(\lambda)$, which were converted to remote sensing reflectance, $R_{rs}(\lambda)$, across visible wavelengths at 410, 443, 486, 551, 638, and 671 nm on SNPP VIIRS, and 411, 445, 489, 556, 642, and 667 nm on NOAA-20 VIIRS, and Level-2 quality flags. Flag exclusion criteria were applied to pixels meeting any of the following conditions: land, cloud, sea ice, atmospheric correction failure, stray light (except for LISCO), bad navigation quality, high or moderate glint, viewing angles exceeding 60°, and solar zenith angles exceeding 70°. Selection of files required at least > 50% valid pixels in a given set, i.e., to be free of flagged conditions. Additionally, pixels with negative water-leaving radiance were excluded from averaging. In matchups of satellite to *in-situ* data from 1 pixel closest to *in-situ* measurements was considered and a 3×3-pixel grid box (2250 m × 2250 m) centered at the AERONET-OC site for the comparison with AERONET-OC data (Hlaing et al., 2013; Gilerson et al., 2022). The average $R_{rs}(\lambda)$ and standard deviation (STD) between pixels, along with their geometric and radiometric properties, were recorded. The bidirectional reflectance distribution function (BRDF) have been applied to the MSL12-derived VIIRS ocean color data as well as to OLCI data with MSL12 processing (Gordon, 2005; Wang, 2006; IOCCG, 2010).

2.2.2 OLCI data

The OLCI S3A and S3B Level-2 full-resolution data with 300-meter spatial resolution per pixel (EUMETSAT, 2021; Mikelsons et al., 2022) with the Operational Baseline Collection-3 (OBC-3) processing (Zibordi et al., 2022) were acquired from the NOAA CoastWatch website (https://coastwatch.noaa.gov/cwn/index.html), focusing on the Chesapeake Bay area and Long Island Sound. Each Level-2 file encompasses various geophysical products related to the atmosphere and ocean, including aerosol optical thickness, Angstrom exponent at 865 nm, water-leaving reflectance at 413, 443, 490, 560, 665, 681, and 709 nm, sensor zenith angle, solar zenith angle, and quality flags. The remote sensing reflectance, R_{rs} (λ), is computed by dividing the reflectance spectra by π.

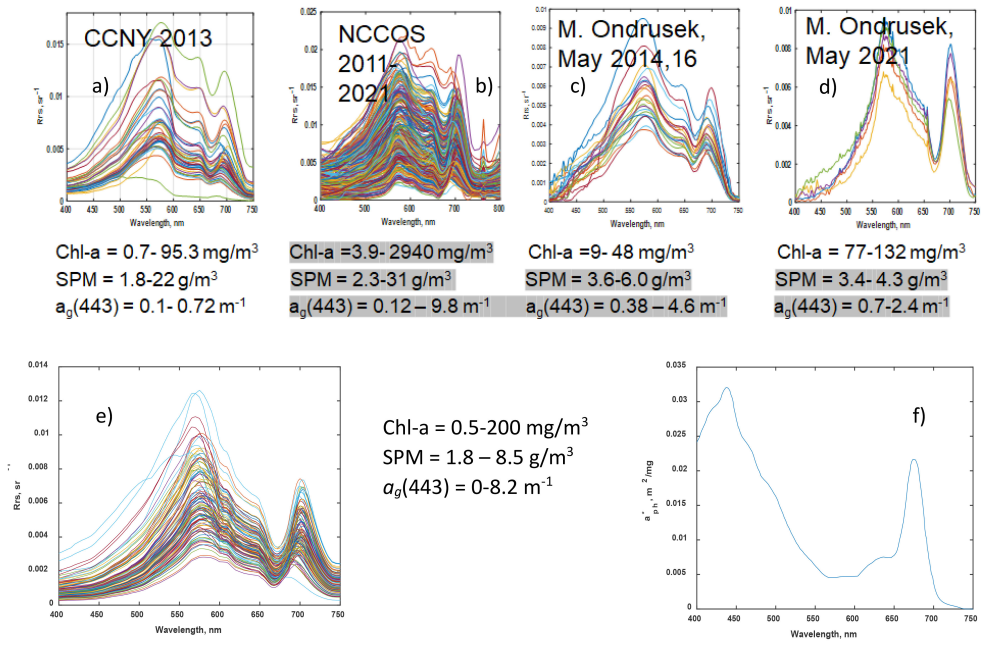

FIGURE 1
Available field R_{rs} datasets **(A–D)** and examples of simulated datasets **(E)** with main water parameters; based specific phytoplankton absorption $a^*_{ph}(\lambda)$ (Magnuson et al., 2004) used in the model **(F)**. Unshaded parameters are measured **(A, C, D)** or simulated **(E)**. Shaded parameters are estimated from different algorithms.

OLCI Level-2 operational water reflectance products do not include BRDF correction. This omission is due to historical usage patterns, with primary interest focusing on coastal and inland waters where the standard open-ocean BRDF approach is not applicable. Mikelsons et al. (2022) showed that there are some significant BRDF effects, both on the surface (Gordon, 2005; Wang, 2006) and in water BRDFs (IOCCG, 2010), over open oceans. However, because there are no established BRDF correction algorithms for a wide range of coastal waters considered in this work, BRDF correction was not applied.

Pixels flagged under any of the following conditions were excluded: invalid flag, land, cloud (including ambiguous and marginal), coastline, solar zenith angle exceeding 70°, saturated flag, moderate or high glint, whitecaps, and failed atmospheric correction. It is important to note that this flag set differs slightly from the set recommended by EUMETSAT for OLCI (EUMETSAT, 2022). A file was selected if at least 50% of valid pixels in the set were free of flags. As for VIIRS, a comparison with measured *in-situ* Chl-a was carried out for 1 closest pixel and for comparison with AERONET-OC 7×7 (2100 m × 2100 m) pixel box was considered.

R_{rs} uncertainties from OLCI in the blue part of the spectra in EUMETSAT atmospheric correction processing are higher than those from VIIRS, especially in coastal waters (Zibordi et al., 2022; Mikelsons et al., 2022; Gilerson et al., 2023). NOAA NCCOS considered a special atmospheric correction (Wynne et al., 2018) using SeaDAS and the subtraction of the Rayleigh component from the TOA radiance. Later, OLCI TOA data were processed using NOAA MSL12 and NASA l2gen algorithm. All these processing schemes were considered with a focus on $R_{rs}(\lambda)$ at the red/NIR bands necessary to apply the RE10 algorithm for the detection of algal blooms.

2.3 AERONET-OC data

Remote sensing reflectance (R_{rs}) for VIIRS and OLCI satellite sensors were assessed through comparisons with SeaPRISM instrument (CIMEL Electronique, France) data at the Chesapeake Bay and Long Island Sound (LISCO) stations, where SeaPRISM radiometers are deployed on offshore fixed platforms and are part of AERONET-OC network (Zibordi et al., 2009, 2021). Normalized water-leaving radiances, $nL_w(\lambda)$, following AERONET-OC protocols and incorporating BRDF correction based on open ocean approaches (Zibordi et al., 2009, 2021), were acquired from the AERONET-OC website for the designated sites. These radiances were transformed into remote sensing reflectance at specific wavelengths. The Long Island Sound Coastal Observatory (LISCO) site (Harmel et al., 2011) upgraded its sensor head in August 2021 to match OLCI sensors with bands at 412, 443, 490, 510, 560, 620, 667, 681, and 709 nm, for detailed comparisons with OLCI data.

The ocean color data employed in this analysis were derived from version 3 level 1.5 data, which underwent cloud screening and quality control measures to ensure data accuracy. All satellite-to-*in situ* matchups were conducted within a ±2-hour window around the satellite overpass time (Zibordi et al., 2009, 2021).

2.4 Bio-optical model

To develop the NN algorithm, datasets, which connect Chl-a, IOPs and $R_{rs}(\lambda)$, water reflectance spectra were simulated based on the bio-optical model (Gilerson and Huot, 2017) with $R_{rs}(\lambda)$ including the sum of elastic $R_{rs}^{e}(\lambda)$ component and fluorescence component $R_{rs}^{f}(\lambda)$; the latter was included because it is a part of the reflectance detected by the broad I1 600-680 nm band. $R_{rs}(\lambda)$ spectra were simulated with 1 nm resolution in the range of 400–750 nm. The maximum of the peak of the fluorescence emission was assumed at 685 nm, fluorescence quantum yield was assumed 1%; the spectral shape of fluorescence was modeled as a Gaussian spectral profile centered at 685 nm, having a full width at half maximum (FWHM) of 25 nm (Mobley, 1994; Gower et al., 2004).

Above water elastic $R_{rs}^{e}(\lambda)$ was calculated following Lee et al. (2002):

$$R_{rs}^{e}(\lambda) = 0.52\frac{R_{rs}^{-}(\lambda)}{(1 - 1.7R_{rs}^{-}(\lambda))} \quad (1)$$

where $R_{rs}^{-}(\lambda)$ is the remote sensing reflectance due to elastic scattering just below the surface, which is calculated as:

$$R_{rs}^{-}(\lambda) = g_1 u(\lambda)^2 + g_2 u(\lambda), \quad (2)$$

$$u(\lambda) = b_b(\lambda)/(a(\lambda) + b_b(\lambda)) \quad (3)$$

where $a(\lambda)$ (m^{-1}) and $b_b(\lambda)$ (m^{-1}) are the total absorption and backscattering coefficient spectra, respectively. Broadly used empirically derived parameters (Lee et al., 2009) $g_1 = 0.125$ and $g_2 = 0.089$, which work well for moderate open ocean and coastal waters were replaced with $g_1 = 0.23$ and $g_2 = 0.089$ equivalent to the relationship based on our previous studies for a broader range of water parameters (Gilerson et al., 2007, 2015).

The total spectral absorption coefficient, $a(\lambda)$, is modeled as

$$a(\lambda) = a_w(\lambda) + a_{ph}(\lambda) + a_g(\lambda) + a_{NAP}(\lambda), \quad (4)$$

where the water absorption spectrum $a_w(\lambda)$ was obtained from (Pope and Fry, 1997).

In coastal waters, $a_{ph}(443)$, $a_g(443)$ and $a_{NAP}(443)$ typically have some correlation (even often weak) with each other (IOCCG, 2006). Based on the data from the NOMAD Chesapeake Bay field campaigns (Gilerson et al., 2015) and $a_{ph}^{*}(443)$ spectra in the Upper Chesapeake Bay (Magnuson et al., 2004) the following relationships at 443 nm were used in the model:

$$a_{ph}(443) = a_{ph}^{*}(443)Chl\text{-}a = 0.031Chl\text{-}a^{-0.12}Chl\text{-}a$$
$$= 0.031Chl\text{-}a^{0.88} \text{ for } Chl\text{-}a < 60 \text{ mg/m}^3 \quad (5a)$$

$$a_{ph}(443) = a_{ph}^{*}(443)Chl\text{-}a = 0.019Chl\text{-}a \text{ for } Chl\text{-}a > 60 \text{ mg/m}^3 \quad (5b)$$

$$a_g(443) = 1.1a_{ph}(443) \quad (6)$$

$$a_{NAP}(443) = 1.32 \times 0.04Chl\text{-}a^{0.65} \quad (7)$$

According to Equation 5, $a^*_{ph}(443)$ gradually decreases with Chl-a and remains constant after 60 mg/m^3. $a_g(443)$ mostly followed $a_{ph}(443)$ and $a_{NAP}(443)$ increases with Chl-a, but less fast than Chl-a itself.

Chl-a were randomly distributed between 0.5 and 200 mg/m^3. The spectral phytoplankton absorption coefficient was obtained by multiplying the Chl-a by a specific absorption coefficient ($a^*_{ph}(\lambda)$, m^2 mg^{-1}),

$$a_{ph}(\lambda) = Chl\text{-}a \times a^*_{ph}(\lambda). \quad (8)$$

The choice of $a^*_{ph}(\lambda)$ strongly influences the corresponding remote sensing reflectance and the emission of fluorescence and was modeled as the specific phytoplankton absorption coefficient in the Upper Chesapeake Bay (Magnuson et al., 2004), shown in Figure 1F with a gradual decrease with increasing Chl-a consistent with Equation 5.

To simulate natural variability, $a^*_{ph}(443)$ were multiplied by a random number drawn from a normal distribution ($N(\mu, \sigma^2)$) with a mean μ=1 and a variance σ^2=0.04: $X_1 \sim N(1, 0.04)$. In a similar manner, $a_g(443)$ and $a_{NAP}(443)$ in Equations 6 and 7 were multiplied by $X_2 \sim N(1, 0.09)$. The ranges of variability here and below were based primarily on the published values from IOCCG (2006), NOMAD and the authors' data for the Chesapeake Bay (Gilerson et al., 2015).

The spectral absorption coefficients of both CDOM and NAP were modeled as having an exponentially decreasing shape with wavelength and referenced to 443 nm (Bukata et al., 1995; Stramski et al., 2001):

$$a_g(\lambda) = a_g(443)e^{-S_g(\lambda-443)}, \quad (9)$$

$$a_{NAP}(\lambda) = a_{NAP}(443)e^{-S_{NAP}(\lambda-443)}. \quad (10)$$

S_g was modeled as a normal distribution $0.017N(1, 0.02^2)$ and S_{NAP} as $0.010N(1, 0.01^2)$. Equation 7 was also used to determine the concentration of NAP, [NAP] (g m^{-3}):

$$[NAP] = a_{NAP}(443)/a^*_{NAP}(443), \quad (11)$$

where $a^*_{NAP}(443)$ (m^2 g^{-1}) is the mass-specific absorption coefficient of NAP at 443 nm, which was simulated as a uniformly distributed random number $0.03 \le a^*_{NAP}(443) \le 0.05$ (m^2 g^{-1}). The [NAP] was typically in the range of 0–30 g m^{-3}.

The total scattering coefficient ($b(\lambda)$, m^{-1}) was simulated as a sum of three components:

$$b(\lambda) = b_w(\lambda) + b_{ph}(\lambda) + b_{NAP}(\lambda). \quad (12)$$

Scattering by NAP was modeled using a power law function (Stramski et al., 2001; Twardowski et al., 2001) as follows:

$$b_{NAP}(\lambda) = b_{NAP}(550)\left(\frac{550}{\lambda}\right)^{\gamma_2}, \quad (13)$$

$$b_{NAP}(550) = b^*_{NAP}(550)[NAP], \quad (14)$$

where $b^*_{NAP}(550) = 0.5N(1, 0.04)$ (m^2 g^{-1}) is the mass-specific scattering of non-algal particles at 550 nm, and $\gamma_2 = 0.8N(1, 0.0049)$.

The scattering by phytoplankton was calculated as the difference between their attenuation and absorption coefficients (Voss, 1992; Roesler and Boss, 2003):

$$b_{ph}(\lambda) = c_{ph}(\lambda) - a_{ph}(\lambda). \quad (15)$$

The attenuation coefficient itself was modeled as a power law function (Voss, 1992),

$$c_{ph}(\lambda) = c_{ph}(550)\left(\frac{550}{\lambda}\right)^{\gamma_1}, \quad (16)$$

where $c_{ph}(550) = 0.3Chla^{0.57}$ and $\gamma_1 = 0.8$.

In the simulations, the backscattering coefficient ($b_b(\lambda)$, m^{-1}) was modeled as the sum of the contributing components,

$$b_b(\lambda) = b_{bw}(\lambda) + \tilde{b}_{b\,ph}b_{ph}(\lambda) + \tilde{b}_{b\,NAP}b_{NAP}(\lambda), \quad (17)$$

where $b_{bw}(\lambda)$ is obtained according to Morel, 1974 and $\tilde{b}_{b\,ph}$ and $\tilde{b}_{b\,NAP}$ are backscattering ratios for phytoplankton and non-algal particles assumed to be independent of the wavelength (Twardowski et al., 2001; Sydor and Arnone, 1997). Typical values were used as $\tilde{b}_{b\,ph}(\lambda) = 0.006$ and $\tilde{b}_{b\,NAP}(\lambda) = 0.02$.

120000 different conditions were simulated using this model with 70% used in generation and 30% in testing and validation.

As was discussed above, several field R_{rs} datasets were available for analysis together with (or without) some measurements of water parameters. Four R_{rs} sets are shown in Figure 1 with corresponding water parameters; some of these parameters (shown in grey) were not measured directly but estimated using available algorithms. Examples of simulated R_{rs} spectra are also shown in this figure. It should be noted that there was a relatively small flexibility in the selection of parameters described above, which produce spectra similar to the ones in the bloom areas with typical high CDOM and corresponding low R_{rs} in the blue, spectral features in green-red and a very strong peak around 700 nm comparable with the peak in the green.

In the model development, $R_{rs}(\lambda)$ spectra were supposed to be similar not only to the field spectra in Figure 1, but there were also supposed to be consistent with the good performance of blue-green algorithms for Chl-a retrievals. This should be true at least in the waters with low to moderate Chl-a and RE10 NIR/red bands algorithm for a broad range of waters and Chl-a concentrations, which were observed previously for the Chesapeake Bay (Gilerson et al., 2015).

The ranges of water parameters in the Chesapeake Bay are Chl-a = 0.06–165 mg/m^3, CDOM absorption at 443 nm $a_g(443)$ = 0.015–2.0 m^{-1}, absorption of non-algal particles $a_{NAP}(443)$ = 0.001–3.0 m^{-1}, scattering at 443 nm $b(443)$ = 0.3–40.3 m^{-1} with the lowest value typically in the Lower Bay and the highest in the Upper Bay (Magnuson et al., 2004). For LIS Chl-a = 1–25 mg/m^3, $a_g(440)$ = 0.012–0.5 m^{-1}, $a_{NAP}(440)$ = 0.02–0.42 m^{-1}, particulate backscattering at 650 nm b_{bp} = 0.005–0.06 m^{-1} with the lowest value in the eastern part of the Sound and the highest in the western part (Aurin et al., 2010). In the model Chl-a values were randomly distributed between 0.5 and 200 mg/m^3, $a_g(443)$ were mostly in the range of 0–3 m^{-1} with decreasing quantities till 6.5 m^{-1} and $a_{NAP}(443)$ = 0–2.5 m^{-1}.

Several metrics were used in the evaluation of Chl-a algorithms performance which includes a coefficient of determination R^2, root

mean square error (RMSE), relative error e = RMSE/mean as well as recently suggested metrics (Seegers et al., 2018) mean absolute error

$$MAE = 10 \wedge \left(\frac{\sum_{i=1}^{n} |\log_{10}(M_i) - \log_{10}(Q_i)|}{n} \right), \quad (18)$$

and bias

$$bias = 10 \wedge \left(\frac{\sum_{i=1}^{n} \log_{10}(M_i) - \log_{10}(Q_i)}{n} \right). \quad (19)$$

It should be noted that in some figures Chl-a values are shown in the logarithmic scale, while RMSE and e were calculated based on the linear scale.

2.5 NN algorithm development, analysis of the optimized structure and validation

In continuation of the approach used by (El-Habashi et al., 2016), their simple one-hidden layer multilayer perceptron (MLP) structure was first applied to a newly developed synthetic dataset, to produce a minimum benchmark against which to improve with the introduction of the VIIRS imaging I1 band to complement the 486, 551 and 671 nm band inputs as well as with modifications to the neural network itself. Variables $a_{ph}(443)$, $a_g(443)$, $a_d(443)$ and $b_b(443)$ were kept as outputs. Chl-a was determined also as an independent output parameter. Performance results are visible in Table 1. The introduction of the imaging I1 band immediately provided a large performance boost on all four output parameters. However, changes in the neural network structure with the introduction of more neurons in the single hidden layer and the introduction of Rectified Linear Units (ReLU) as the activation function produced a negligible change in the network performance. Similarly, the introduction of a second hidden layer also produced a negligible change in the network performance, indicating that the simpler neural network utilized in previous studies is already capable of capturing the relationships between inputs and outputs well.

In original tests, the bio-optical model was slightly different from the one described above (specific phytoplankton absorption consisted of the micro- and picoplankton absorption with a weighting factor from Ciotti and Bricaud, 2006). In the final version, R^2 coefficients were higher as shown in Table 1 in parentheses. Figure 2 contrasts the performance of the NNs in the 3-band and 4-band versions against the expected values for $a_{ph}(443)$, $a_g(443)$, $a_d(443)$, and $b_b(443)$ as measured during the CCNY 2013 cruise in the Chesapeake Bay. In all cases, including the VIIRS imaging I1 band noticeably improves the retrieval quality. In these tests, Chl-a were determined from $a_{ph}(443)$. When Chl-a were used directly as one of the retrieval parameters, R^2 for Chl-a became 0.984.

If large datasets of Chl-a and R_{rs} are available for relevant water conditions, the training can be carried out directly to retrieve Chl-a and other water parameters from R_{rs} spectra (Hieronymi et al., 2017; Pahlevan et al., 2020). While only 70 points of the field data were available for the Chesapeake Bay, the training gave results quite similar to the ones from the bio-optical modeling, however, some additional tuning was still required, and this option was not further explored.

3 Results

3.1 Preliminary studies

3.1.1 Performance of different Chl-a algorithms

A Satlantic HyperSAS (Halifax, Canada) system was installed from 2009 to 2014 at the LISCO site (Harmel et al., 2011) together with the SeaPRISM instrument on top of a retractable tower at approximately 12 m above the water surface. Three spectrometers observed downwelling irradiance E_d, sky radiance L_s, and total radiance L_t in the wavelength range of 305–905 nm with 180 equally spaced channels. HyperSAS data were processed by the 3C model (Groetsch et al., 2017, 2020) to minimize the impact of the sky reflectance from the windy surface and to produce reliable R_{rs} data. Several algorithms to determine Chl-a were applied to analyze water conditions in the area of LISCO during the year of 2013, which included conditions of algal blooms. Algorithms included standard 3 bands OC3V algorithm (based on 443, 486 and 551 nm), 6 bands OC6P algorithm (O'Reilly and Werdell, 2019), NN algorithm (El-Habashi et al., 2019), and NIR/red (red edge) (Gilerson et al., 2010), further referred to as RE10, based on $R_{rs}(709)/R_{rs}(665)$ ratio. The latter algorithm proved to perform well in a very broad range of Chl-a > 5 mg/m^3 and other water components (Smith et al., 2018; Pahlevan et al., 2022). All algorithms except RE10 performed similarly at Chl-a < 10 mg/m^3 and substantially underestimated Chl-a in bloom conditions in 2013, where only RE10 indicated Chl-a up to 40 mg/m^3.

3.1.2 R_{rs} uncertainties

It has been well known for a long time that main R_{rs} uncertainties over coastal waters occur at the blue bands 412 and 443 nm (IOCCG, 2019), which motivated the development of other algorithms avoiding the 443 nm band on VIIRS sensors (Ioannou et al., 2014; Gilerson et al., 2015; El-Habashi et al., 2016) and NIR/red algorithms on MERIS and OLCI sensors, which have 709 nm band (Gitelson, 1992; Moses et al., 2009; Gilerson et al., 2010). While main uncertainties in the blue were usually attributed to inaccurate aerosol models in the atmospheric correction process (IOCCG, 2019), a recent analysis based on the decomposition of R_{rs} uncertainties spectra showed that some uncertainties may be associated with Rayleigh-type components and thus might be related to small variability (about 1.5%) of the Rayleigh radiance (Gilerson et al., 2022, 2023) or Rayleigh noise (Malinowski et al., 2024). It was also shown that OLCI uncertainties in coastal waters in EUMETSAT processing are about 50% higher than uncertainties for VIIRS in the blue (Mikelsons et al., 2022; Zibordi et al., 2022; Gilerson et al., 2023) due to the different atmospheric correction schemes (Mikelsons et al., 2022) with NOAA MSL12 OLCI processing having R_{rs} uncertainties about the same as for VIIRS. Further, NASA OLCI processing also showed the same level of uncertainties as those from VIIRS and NOAA MSL12 OLCI. These effects are additionally demonstrated in Figure 3, where matchups

TABLE 1 Performance summary in R^2 of the neural networks tested on the synthetic dataset, original (final) bio-optical model.

Description	Network structure	Activation	$a_{ph}(443)$	$a_g(443)$	$a_d(443)$	$b_b(443)$
Original MLP	3 × 6 × 4	Sigmoid	0.601 (0.726)	0.588 (0.753)	0.546 (0.738)	0.555 (0.635)
I1 band	4 × 6 × 4	Sigmoid	0.722 (0.80)	0.796 (0.823)	0.640 (0.807)	0.749 (0.77)
More neurons	4 × 36 × 4	ReLU	0.719	0.794	0.635	0.743
2 hidden layers	4 × 36 × 30 × 4	ReLU	0.722	0.798	0.639	0.746

are shown for VIIRS, OLCI EUMETSAT, and OLCI MSL12 data processing at the LISCO AERONET-OC site.

High uncertainties can be clearly seen at the 443 nm band for VIIRS with a much more stable 490 nm band. Results are similar in OLCI MSL12 data processing. In EUMETSAT data processing, all bands below 560 nm show high uncertainties. Uncertainties at 665 nm and 709 nm are also high but these R_{rs} are related to low Chl-a < 10 mg/m^3 conditions in LIS, they are not of the main interest for the application of the NIR/red algorithm, which works reliably mostly for higher Chl-a. At the Chesapeake Bay AERONET-OC station with waters clearer around the AERONET-OC station than at the LISCO site, correlations were higher for OLCI (not shown).

3.1.3 Evaluation of the performance of Chl-a algorithms in algal bloom conditions

Blooms often occur near salinity fronts in the Upper Bay and Potomac River. Satellite imagery for the Chesapeake Bay with bloom conditions in the Upper Bay, processed with OC3V for VIIRS, with RE10 using EUMETSAT OLCI imagery with default and NCCOS atmospheric corrections together with the Chl-a distributions received with an additional band ratio algorithm. Chl-a in the bloom areas from different algorithms were 27–140 mg/m^3 for the Upper Bay and 30–200 mg/m^3 for the Potomac River. These data had to be reconciled between different satellite sensors and algorithms to develop a combined VIIRS-OLCI product for bloom detection.

At the beginning, Chl-a were estimated in the bloom areas in the Chesapeake Bay and in the Potomac River for May 13, 2020, using four different algorithms, including the standard three bands OC algorithm for VIIRS OC3V, the band ratio VIIRS algorithm with I1 band (chlC) (Gilerson et al., 2021) described below in Section 3.1.4, OLCI RE10 algorithm with standard OLCI AC and with NCCOS AC (Wynne et al., 2018). Two bloom areas have been identified: in the Upper Bay and in the Potomac River. While the shapes of the bloom areas on satellite images looked similar, it was found that OC3V had the lowest Chl-a values around 30 mg/m^3 and RE10 = 50 – 140 mg/m^3 in the Upper Bay and above 200 mg/m^3 in the Potomac River with chlC values were in the middle of these ranges. The focus of this work was a more detailed evaluation of these algorithms and the newly developed NN algorithm in various bloom conditions.

3.1.4 Band ratio algorithm with I1 band

The first tests (Gilerson et al., 2021) proved the utility of I1 band in detecting higher concentrations of Chl-a values. Because of the

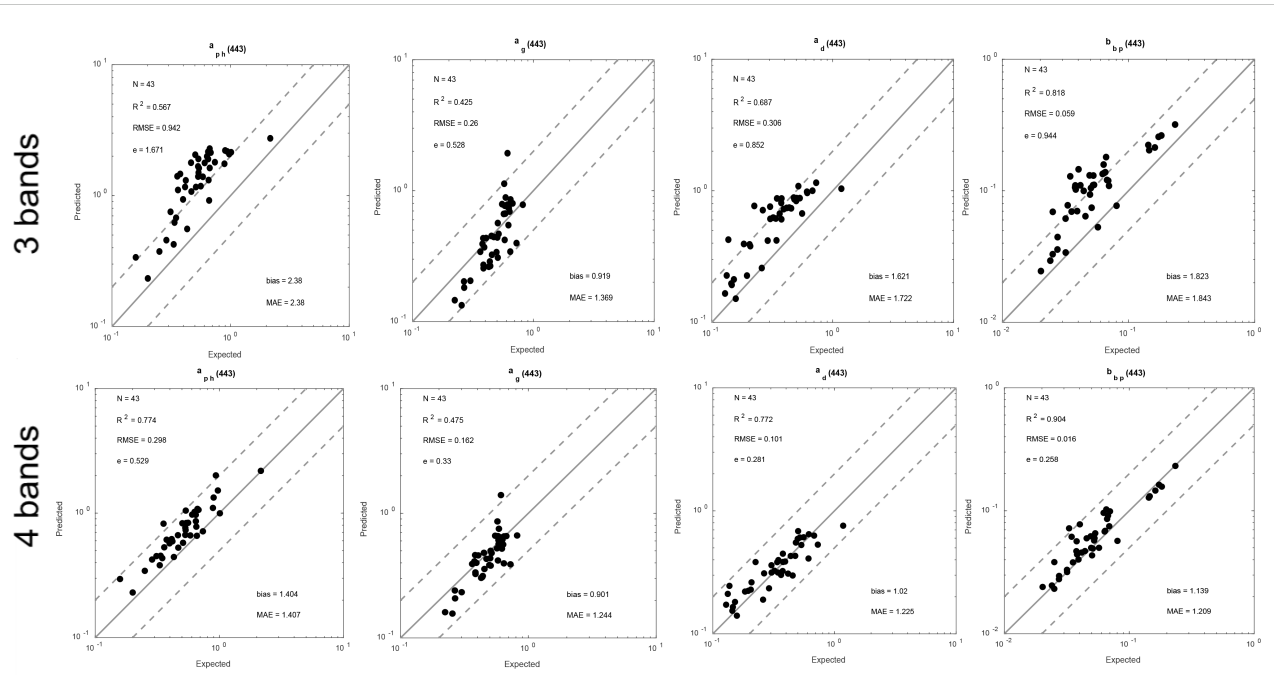

FIGURE 2
Results of a and b_b retrievals in m^{-1} using NN with 3 bands (top) and 4 bands (bottom) based on field data from CCNY 2013 cruise.

10.3389/fmars.2024.1476425

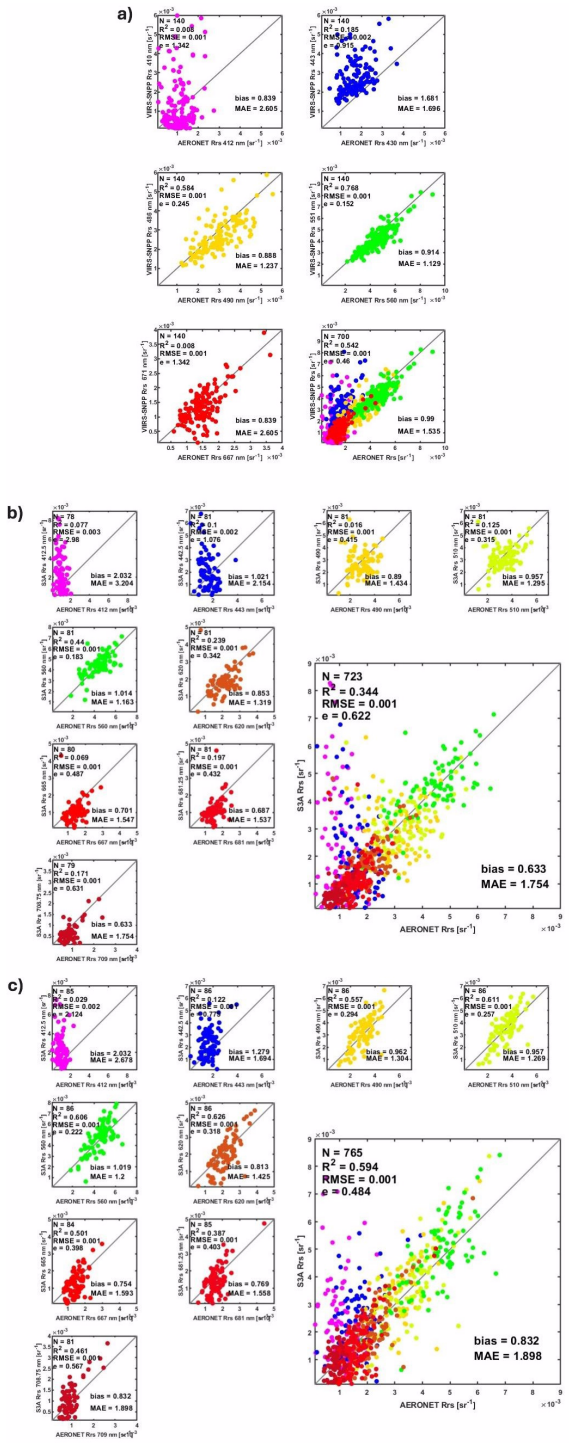

FIGURE 3
Satellite and AERONET-OC matchups at the LISCO site for the matching wavelengths available on the SeaPRISM and on the sensor: **(A)** SNPP VIIRS, **(B)** S3A OLCI with EUMETSAT (OBC-3), and **(C)** S3A OLCI with NOAA MSL12 data processing.

complexity of water IOPs spectra in the I1 range, including variability of CDOM and mineral concentrations in various areas, it was clear that the algorithm eventually needs to be implemented in a NN format. But, it appeared useful to evaluate a multi-band algorithm for the estimation of Chl-a in a wide range of water conditions. The algorithm was developed using available band ratios, which include I1 band. A proper band combination was determined by tests on the synthetic dataset discussed above.

Application of the first version of the algorithm with I1 band, which was calibrated on the field data showed a strong dependence of the estimated Chl-a on the concentration of suspended particulate matter (SPM) with sediment concentrations estimated

from (Nechad et al., 2010) based on R_{rs} at 671 nm. In the next iteration, the algorithm was corrected for the impact of SPM concentration. It was also found that the algorithm often underestimates Chl-a at Chl-a < 10–15 mg/m^3 and it was therefore combined with the standard OC3V algorithm at Chl-a ≤ 15 mg/m^3.

The algorithm was tuned using MATLAB curve fitting toolbox on 43 R_{rs}-Chl-a combinations from the CCNY 2013 cruise and then further on field data from M. Ondrusek's measurements in 2014-2021 (see Figures 4D and F) with a total of 70 points. It was implemented with the final result as chlC:

$$SPM = 384.11 \times \pi R_{rs}(671)/(1 - \pi R_{rs}(671)/0.1747) + 1.44 \quad (20)$$

$$ratio = (R_{rs}(486) + R_{rs}(551))/R_{rs}(638) \times SPM^{0.3} \quad (21)$$

$$ChlC = k \times 4604 \times ratio^{(-4.252)} \quad (22)$$

$$chlC = ChlC \; if \; ChlC > 10 \; mg/m^3 \quad (23a)$$

$$chlC = OC3V \; if \; ChlC \leq 10 \; mg/m^3 \quad (23b)$$

Coefficient k in Equation 22 is a tuning parameter, which can be further changed. In this version, coefficients are different from the original version (Gilerson et al., 2021), when the algorithm was tuned only on the data from the CCNY 2013 cruise. The performance of the algorithm with k =1.0 is demonstrated below in Figures 4D, F.

3.2 Validation of VIIRS algorithms on satellite and field data

A total of 70 matchups were included in the tests (43 from CCNY 2013, 22 from Ondrusek 2014-16, and 5 from Ondrusek 2021 measurements) for the validation of NN3, NN4 and VIIRS standard OC3V algorithms on the field data collected across the Chesapeake Bay. Results are shown in Figures 4A–C. The performance of chlC and RE10 on the same field dataset is shown in Figures 4D–F. Among the first three algorithms in Figure 4 the NN4 algorithm shows better performance, although it is worse than the performance of chlC, where all points were used in the tuning and RE10, for which 709 nm band is not available on VIIRS. In Figures 4D–F chlC is plotted against field

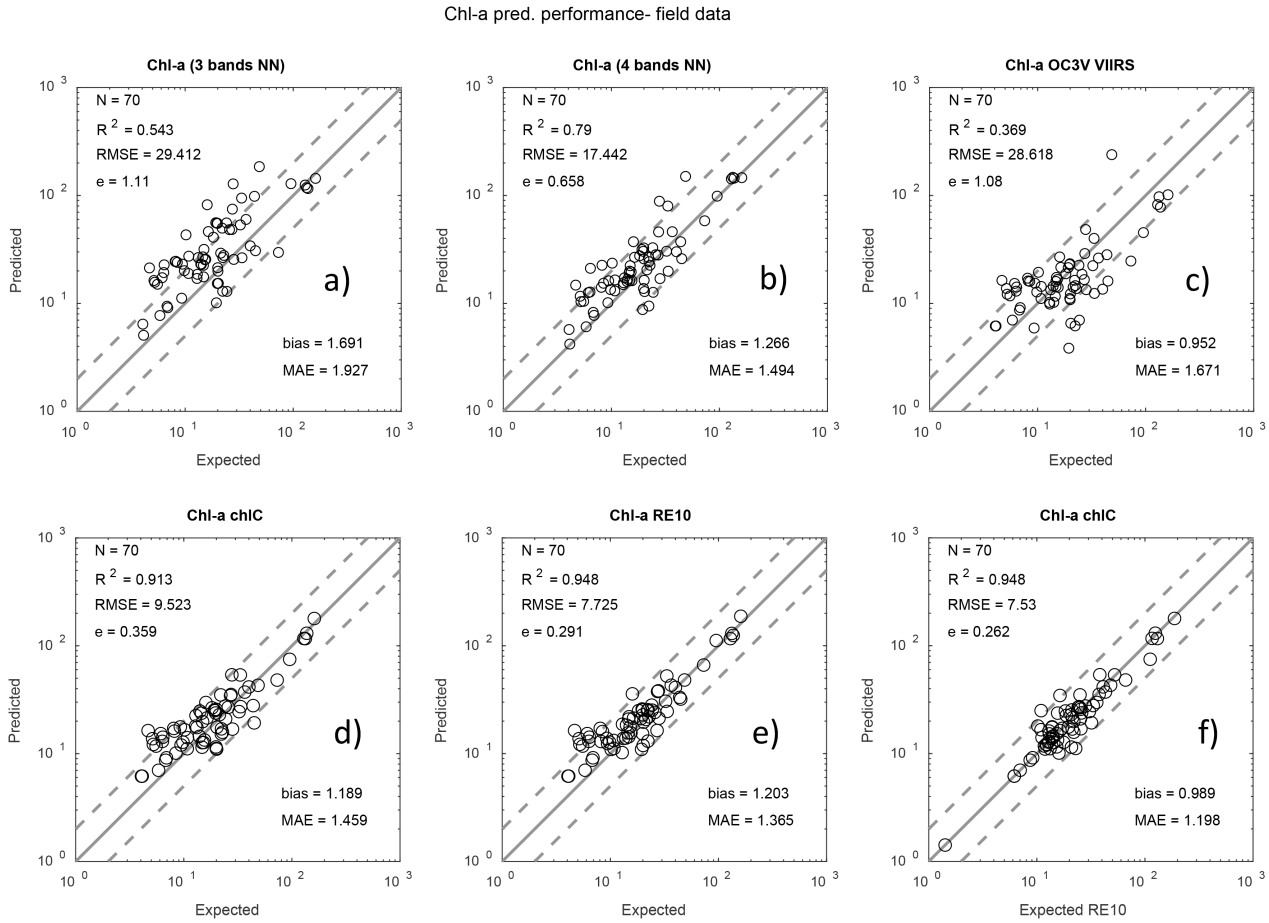

FIGURE 4
Test of algorithms on the field data: **(A)** 3 bands NN; **(B)** 4 bands NN; **(C)** OC3 VIIRS; **(D)** chlC vs *in-situ* Chl-a; **(E)** RE10 vs *in-situ* Chl-a, **(F)** chlC vs RE10.

Chl-a and against RE10; RE10 against Chl-a is also shown for the comparison. High correlations exist for all comparisons in a broad range of conditions in the Chesapeake Bay, but these relationships are not always valid for other types of waters. RE10 was also considered as OC3 VIIRS if RE10 <10 mg/m^3.

RE10 was used with the expression (24), which matches the original version in Gilerson et al., 2010, but does not produce complex numbers at low Chl-a

$$RE10 = 46.0676(R_{rs}(709)/R_{rs}(665))^{1.2260} - 22.6012 \quad (24)$$

Further tests were performed on SNPP VIIRS data 2012–2022 (NOAA MSL12 data processing) compared with *in-situ* data from the Chesapeake Bay program (https://www.chesapeakebay.net) and there were 2021 measurements at 5 locations. Results are shown in Figure 5. The stray light flag was on, HIGLINT and MODGLINT flags were suspended since they did not change the algorithm performance significantly. Most of the points are in the Chl-a range below 20 mg/m^3. However, all algorithms, including the OC3 algorithm, retrieve high Chl-a values reasonably well; good performance of OC3 is most likely due to the specific combination of the water parameters in bloom areas, which is not typical for coastal waters with high Chl-a. The time window between satellite and *in-situ* measurements was ±4 hours. Based on our studies in the Chesapeake Bay, stricter time limits would reduce the number of points but would not improve statistics.

Here and in the figures below the solid grey line marks the 1:1 relationship, while the upper and lower dashed lines mark the limit of Y = X*2 and Y = X/2, respectively, where Y are predicted values and X are expected values.

3.3 Comparison of Chl-a retrievals by VIIRS and OLCI algorithms

Performance of the RE10 algorithm for OLCI sensors was evaluated with NCCOS, EUMETSAT, MSL12 and NASA atmospheric correction by the comparison with VIIRS Chl-a in bloom areas with a very broad range Chl-a from 2 mg/m^3 to over 100 mg/m^3. Because the RE10 algorithm does not provide accurate retrievals for low Chl-a and the OC4 algorithm for OLCI was found not to be always reliable in the waters of the Chesapeake Bay, comparisons were carried out using the RE10M algorithm, where RE10 was replaced with OC3V Chl-a for Chl-a < 6 mg/m^3. It was found that the most consistent matchups between VIIRS and OLCI retrievals come from EUMETSAT and MSL12 processing. Examples of such matchups for the Upper Bay and Potomac River bloom areas are shown in Figure 6. NN4 versus RE10M shows better results than other algorithms. For low Chl-a < 6 mg/m^3, OC3V and chlC matchups with RE10M are along 1:1 line because OC3V retrievals are used in all these cases. Since VIIRS algorithms matchups vs RE10M in EUMETSAT and MSL12 matchups produce similar results, both processing approaches from EUMETSAT and MSL12 were recommended for the combined OLCI product. It should be noted that, according to Mikelsons et al. (2022), EUMETSAT processing is more sensitive to the sun glint, which was shown in our comparisons.

3.4 Combined products, and satellite imagery

Based on the whole study, NN4 VIIRS and OLCI RE10 algorithms were recommended for the combined VIIRS-OLCI product. RE10 was used in combination with OC4 (with OC4 if RE10< 10 mg/m^3 and OC4 <10 mg/m^3 or OC4 < 10 mg/m^3 and clear water conditions based on the diffuse attenuation coefficient threshold $K_d(490)$ < 0.25 m^{-1}). Examples of the imagery from both algorithms are shown in Figure 7 for May 18, 2021, when field measurements were also available at 5 locations with the coordinates shown in Table 2, together with measured Chl-a at these points and retrieved from OC3, chlC, NN3, and NN4 algorithms from VIIRS and RE10 from OLCI. Note that part of the area on the OLCI image is masked because of clouds. As before, a slight overestimation of Chl-a is seen in both images in very turbid waters in the Upper Bay, Delaware Bay, and some tributaries. Adjustment coefficients for chlC, NN3, and NN4 are also given in Table 2. Relative spectral response (RSR) functions were not taken into account in the NN algorithms development to simplify tuning of the algorithms based on the bio-optical model only and comparison with field measurements; for the same reason RSR for the I1 band was considered as RSR = 1.0 for the whole range of wavelengths 600–680 nm. The actual RSR for this

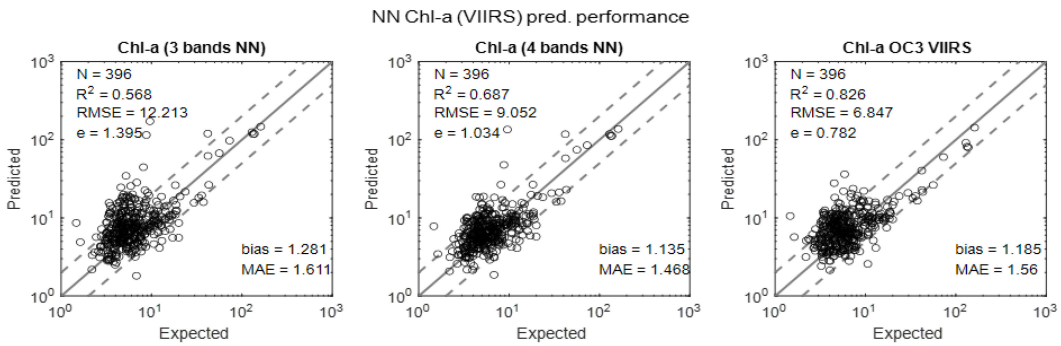

FIGURE 5
Comparison of satellite and *in-situ* data for the Chesapeake Bay. Expected and predicted Chl-a as determined by the one-hidden layer MLP in both its 3-band and 4-band versions and OC3 VIIRS algorithms.

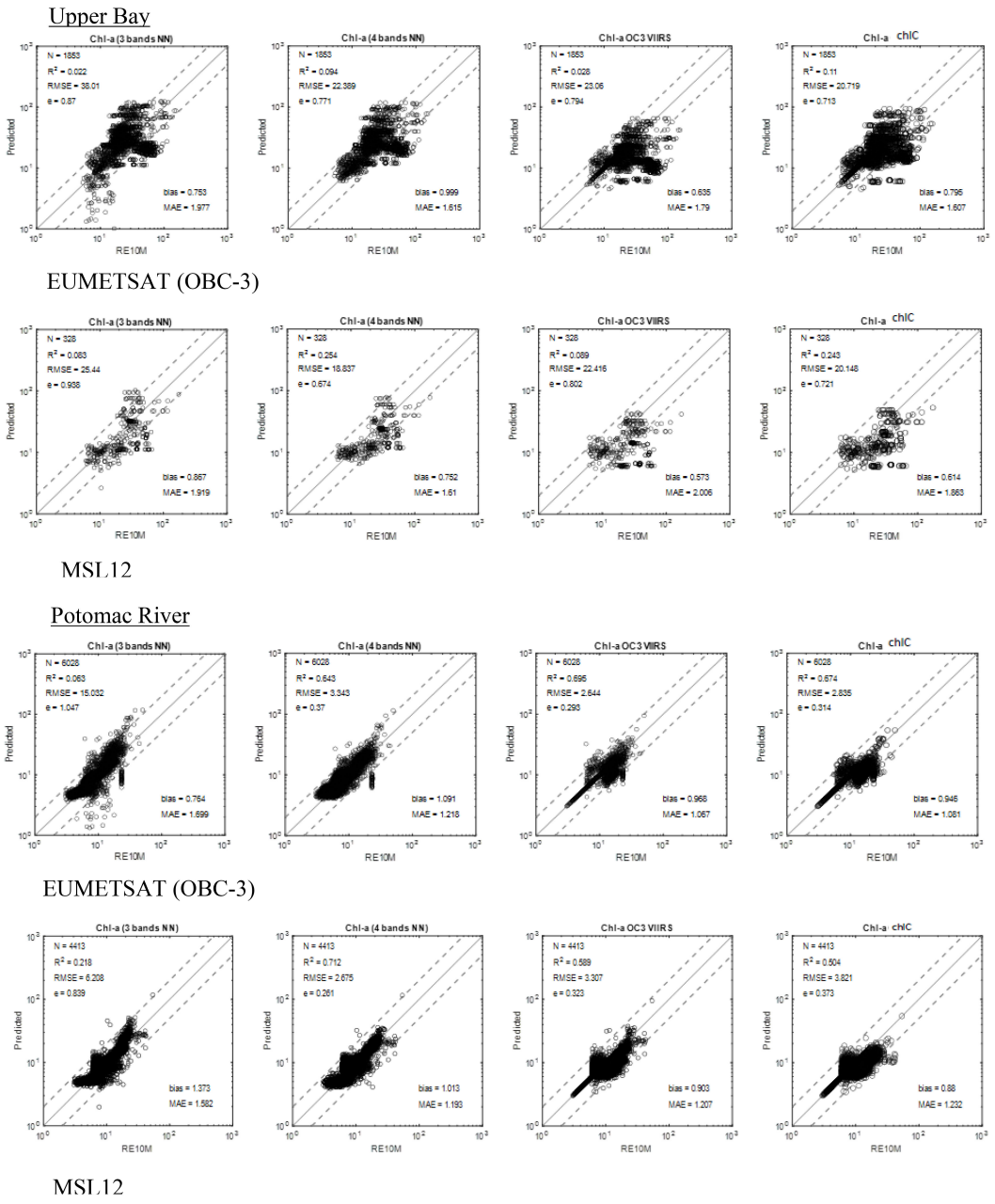

FIGURE 6
Matchups between VIIRS and OLCI Chl-a retrievals in bloom areas.

band is close to RSR ≈ 0.9, which matches the adjustment coefficient for NN4. The NN3 and chlC algorithms provided similar images but with some adjustments of coefficients, which were less stable than those from the NN4 algorithm. Other examples of images from VIIRS and OLCI for bloom conditions on May 21, 2021, and non-bloom conditions on April 4, 2024, are shown in Figure 8.

The distribution of absorption and backscattering coefficients at 443 nm retrieved from NN4 together with the SPM concentration based on Equation 20 for May 18, 2021, are shown in Figure 9, providing additional information about water parameters in the Chesapeake Bay and specifically in the bloom areas, which helps to understand bloom conditions in more details. As can be expected, $a_d(443)$, $b_b(443)$ and SPM have similar patterns since they are mostly proportional to the concentrations of non-algal particles, $a_{ph}(443)$ and $a_g(443)$ are high in the bloom areas.

The NN4 algorithm was developed based on SNPP VIIRS bands, VIIRS on NOAA-20 has several slightly different bands as was shown above, specifically for the NN algorithm there are M3–M5 bands centered at 489, 556, and 667 nm, and I1 band centered at 642 nm and NN4 algorithm required additional tuning. While the effects of

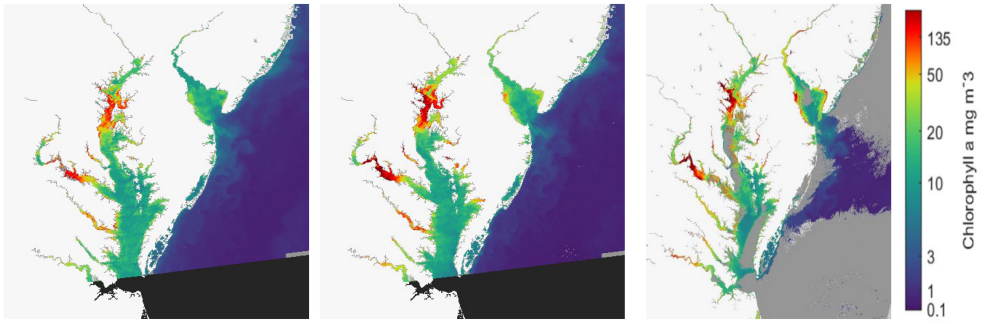

FIGURE 7
OC3 VIIRS (left panel), NN4 VIIRS (middle panel) and OLCI (right panel) Chl-a retrievals in bloom areas on May 18, 2021.

TABLE 2 Chl-a measurements and retrieval comparison for May 18, 2021.

Lat/Lon (West)	Ondrusek	SNPP VIIRS				OLCI	N20 VIIRS	
		OC3V	chlC (1.6)	NN3 (0.85)	NN4 (0.9)	RE10	OC3V	NN4 (0.7)
39.046 76.392	133	82	128	125	126	128	253	110
39.053 76.405	129	91	135	133	133	114	NaN	126
39.055 76.423	161	143	143	156	154	286	NaN	118
39.073 76.403	137	80	121	126	126	164	NaN	163
38.964 76.452	73	60	77	104	96	85	313	104

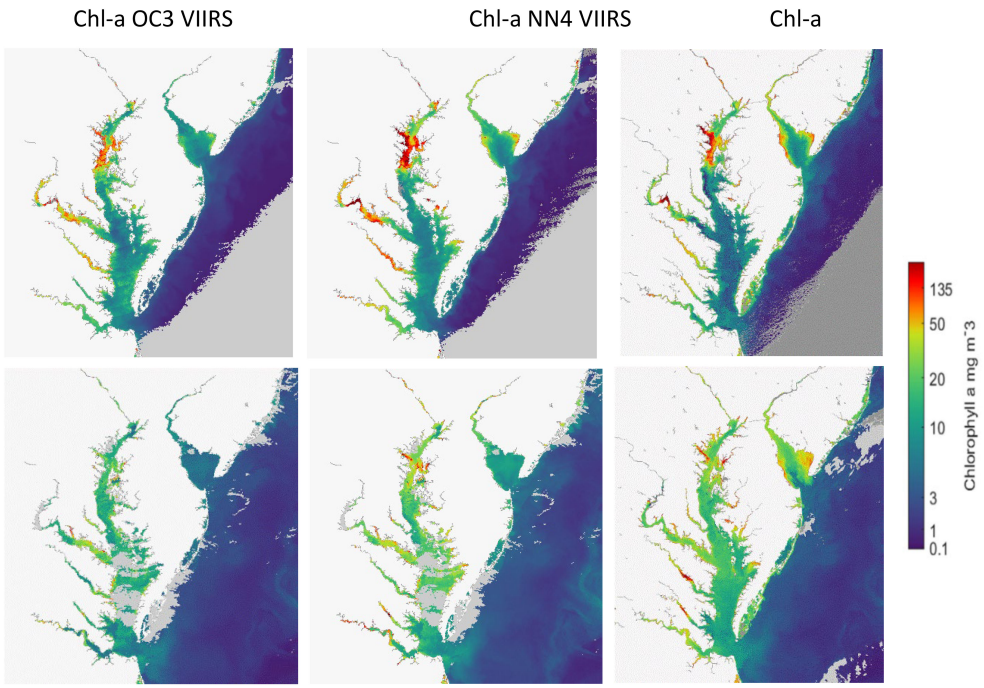

FIGURE 8
OC3 VIIRS, NN4 VIIRS and OLCI Chl-a retrievals with bloom conditions on May 21, 2021 (top row) and non-bloom conditions on April 15, 2024 (bottom row).

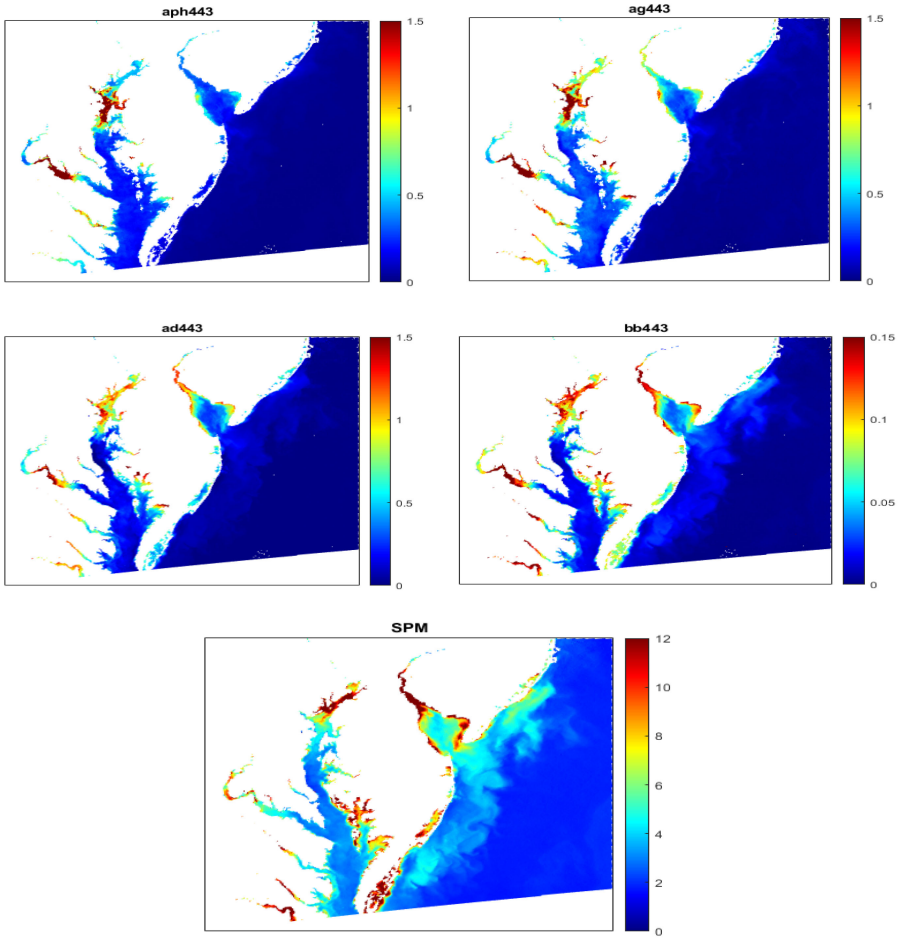

FIGURE 9
Distributions of absorption, backscattering coefficients (m^{-1}), in the Chesapeake Bay from NN4 VIIRS algorithm, SPM (g/m^3) from (NeChad et al., 2010).

spectral differences between VIIRS-SNPP and VIIRS-NOAA-20 at the blue bands are negligible (e.g., within ~0.1% at M2 band), there are large differences at M4 (green) and M5 (red) bands (e.g., ~16% at M4 band for open oceans) (Wang et al., 2020). Over coastal regions, there are important effects of M4 band difference between VIIRS-SNPP and VIIRS-NOAA-20, because R_{rs} from NOAA-20 (at 556 nm) is usually much closer to the R_{rs} peak than that from SNPP (at 551 nm). The same NN4 algorithm was used for VIIRS NOAA-20

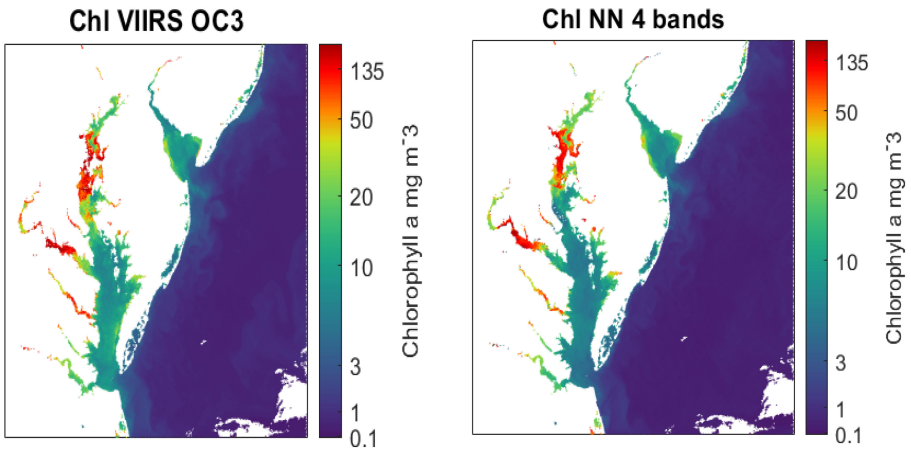

FIGURE 10
Comparison of NOAA-20 VIIRS images retrieved with OC3V and NN4 algorithms.

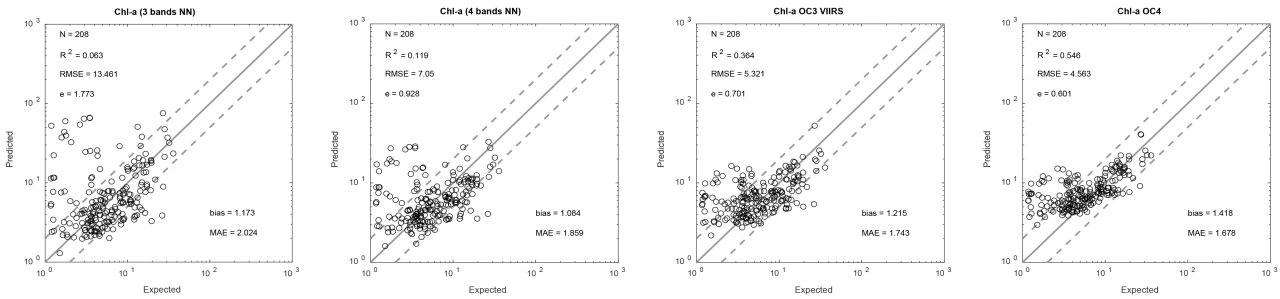

FIGURE 11
Performance of algorithms on R_{rs} and Chl-a data in LIS.

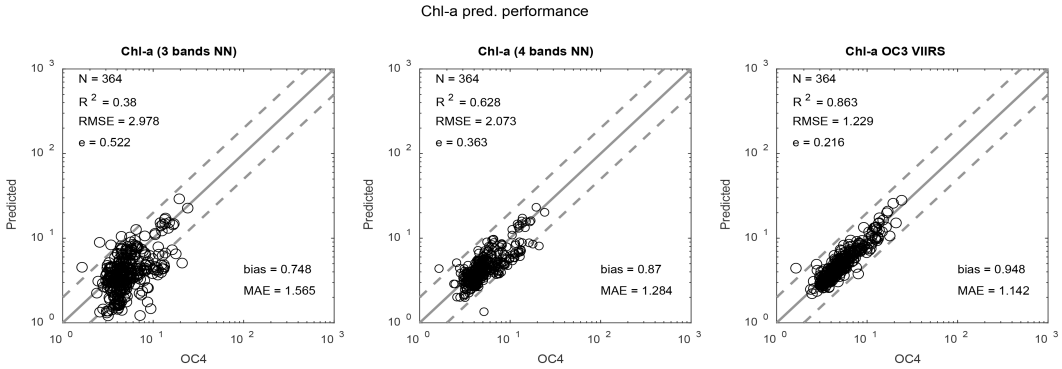

FIGURE 12
Performance of several VIIRS algorithms in comparison with OC4 based on the LISCO radiometric data.

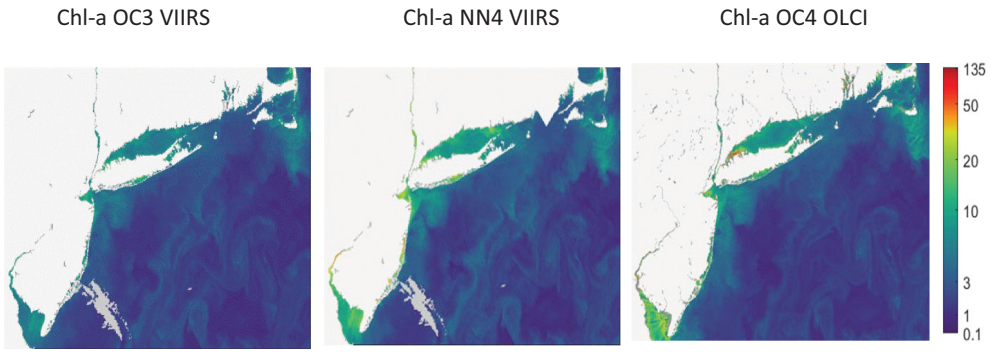

FIGURE 13
OC3, NN4 Chl-a from VIIRS and OC4 from OLCI in LIS on April 16, 2024.

bands but with the coefficient 0.65. Images for OC3V and NN4 for NOAA-20 VIIRS are shown in Figure 10 and Chl-a are added to Table 2. Chl-a from OC3V and NN4 in the same scale looks similar to SNPP Chl-a distributions. For OC3V Chl-a values at *in-situ* measured points match less accurately with a strong overestimation at two points and were not processed at three other points. NN4 for NOAA-20 is less accurate than for SNPP but can be also recommended for the joint product.

3.5 Applications of the developed algorithms to the waters in Long Island Sound

The performance of the NN4 algorithm was validated on the field data in Long Island Sound. Field data were acquired during cruises in 2018–2023 and included radiometric measurements and Chl-a (Sherman et al., 2023). Results for different algorithms are

shown in Figure 11. Most of Chl-a values are below 25 mg/m^3, the range that was not the main focus of the NN4 algorithm. The best performing algorithm is OC4 followed by OC3 and NN4. However, all these algorithms perform quite well for Chl-a > 2 mg/m^3 and much worse below this value. The NN4 algorithm was used with a coefficient of 0.6, while it was 0.9 in the Chesapeake Bay for SNPP VIIRS. The difference in coefficients might be explained by differences in $a^*_{ph}(\lambda)$ with shifts in phytoplankton species (including size and Chl-a packaging), between the time periods in LIS and in the Chesapeake Bay. Optical differences in the water may also influence the bio-optical model. More details about this difference should be further studied.

There were few matchups with VIIRS for field data used in Figure 11. Sherman et al. (2023) had OLCI retrievals corrected with the Polymer atmospheric correction algorithm and a bio-optical model for moderately turbid waters (Steinmetz et al., 2011), which resulted in good agreement with field observation across the Sound. The performance of algorithms was evaluated at the LISCO site for the period of August 2021–May 2022. The SeaPRISM instrument has bands similar to OLCI bands, and there were no direct field Chl-a measurements. Chl-a were estimated by the OC4 algorithm and compared with those from the NN4 and OC3 algorithms with VIIRS bands, with R_{rs} determined from the SeaPRISM bands using an adjustment based on the relationship between bands from the synthetic dataset. The NN4 and OC3 algorithms perform very consistently in the whole range of Chl-a from 2–25 mg/m^3 as shown in Figure 12. However, there were no *in-situ* Chl-a data to confirm these retrievals. Images of Chl-a in LIS based on OC3 and NN4 retrievals for VIIRS and OC4 for OLCI are shown in Figure 13 and are very consistent with each other generally confirming the good performance of algorithms in Figure 12. Both NN4 and OC3 algorithms for VIIRS can be recommended for the joint product with OLCI OC4.

4 Discussion and conclusions

Satellite data and imagery from SNPP and NOAA-20 VIIRS sensors and Sentinel-3A and 3B OLCI sensors were analyzed together with field data to develop the combined product for the estimation of Chl-a in two large US estuaries: the Chesapeake Bay and Long Island Sound to improve detection of algal blooms. The bio-optical model was developed to satisfy a broad range of conditions in waters from low Chl-a and corresponding absorption and backscattering coefficients in fresher reaches of the estuaries, with a switch for higher values in areas with high Chl-a and phytoplankton bloom conditions. The neural network (NN4) algorithm was developed for the retrieval of Chl-a and other water parameters from VIIRS in the Chesapeake Bay, which reasonably matches *in-situ* data. All VIIRS imagery used was from NOAA processing using MSL12 atmospheric correction. Based on the long-time knowledge about the vulnerability of the R_{rs} at 412 and 443 nm bands over coastal turbid waters, these bands were excluded from potential algorithms. The NN4 algorithm utilizes SNPP VIIRS four bands centered at 486, 551, 638, and 671 nm, which includes data from the imaging I1 600-680 nm band centered at 638 nm. It is demonstrated that the inclusion of this band data significantly improved retrieval of Chl-a and other water parameters in comparison with the previous versions of similar algorithms, which utilized only three 486, 551, and 671 nm bands. Analysis of several atmospheric correction and processing approaches from EUMETSAT (OBC-3), NOAA (MSL12), and NASA (L2gen) for OLCI for the application of the NIR/red RE10 Chl-a algorithm that requires accurate R_{rs} values at 665 and 709 nm bands showed that both MSL12 and OBC-3 data can be recommended for the combined product.

The NN4 and RE10 algorithms were analyzed in various water types demonstrating consistency during algal bloom conditions. These algorithms were selected for the multi-sensor product to support algal bloom detection in the Chesapeake Bay. The OC4 algorithm replaces RE10 for Chl-a < 10 mg/m^3, so VIIRS and OLCI Chl-a retrievals are consistent for the broad range of conditions in the Chesapeake Bay. The R_{rs} from the bio-optical model were re-trained to develop a NN4 algorithm for NOAA-20 VIIRS, which showed mostly Chl-a similar to those from the NN4 for SNPP VIIRS. In LIS during the whole period of study, there were no *in-situ* Chl-a above 30 mg/m^3. The NN4, OC3 and OC4 algorithms showed approximately the same performance and can be recommended for the estimation of Chl-a in LIS with the switch to RE10 for OLCI in case of higher Chl-a.

Further examination is recommended to determine if the combined NN4, OLCI with a switch to OC4 under low Chl-a conditions is accurate and provides the best estimate of Chl-a when switching water classes from coastal to offshore. This ability to provide consistent Chl-a from coastal to offshore, with improved cloud clearing capability through a multi-sensor approach, would support improved fisheries modeling capability, improved bloom monitoring, and the development of an improved long-time-series data of Chl-a to determine changes in primary productivity under changing climate conditions and in response to managing nutrient loading into coastal systems.

Data availability statement

The raw data supporting the conclusions of this article will be made available by the authors, without undue reservation.

Author contributions

AG: Writing – original draft, Writing – review & editing, Conceptualization, Funding acquisition, Investigation, Methodology, Project administration, Software, Supervision, Validation. MM: Investigation, Software, Validation, Writing – review & editing. JA: Conceptualization, Investigation, Methodology, Software, Writing – review & editing. EH-E: Investigation, Software, Validation, Writing – review & editing. MTz: Conceptualization, Data curation, Investigation, Methodology, Validation, Writing – review & editing. MTo: Conceptualization, Data curation, Investigation, Methodology, Validation, Writing – original draft, Writing – review & editing. AM:

Data curation, Investigation, Software, Validation, Writing – review & editing. RS: Writing – original draft, Writing – review & editing, Conceptualization, Funding acquisition, Investigation, Methodology, Project administration, Supervision, Validation. MO: Data curation, Investigation, Methodology, Validation, Writing – review & editing. LJ: Investigation, Software, Validation, Writing – review & editing. MW: Conceptualization, Funding acquisition, Investigation, Methodology, Supervision, Validation, Writing – review & editing.

Funding

The author(s) declare financial support was received for the research, authorship, and/or publication of this article. This research was supported by the Joint Polar Satellite System (JPSS) funding including NOAA grant NA19NES4320002 (CISESS). We thank EUMETSAT for providing OLCI Level-1B data and ocean color products. AG, MM and EH-E were also supported by NASA award 80NSSC21K0562 and NOAA CESSRST center.

Acknowledgments

The authors are grateful to the reviewers, whose comments led to the significant improvement of the manuscript.

Conflict of interest

Author AM was employed by the company Consolidated Safety Services, Inc.

The remaining authors declare that the research was conducted in the absence of any commercial or financial relationships that could be construed as a potential conflict of interest.

Publisher's note

Author disclaimer

The scientific results and conclusions, as well as any views or opinions expressed herein, are those of the author(s) and do not necessarily reflect those of NOAA or the Department of Commerce.

References

Anderson, T. H., and Taylor, G. T. (2001). Nutrient pulses, plankton blooms, and seasonal hypoxia in western Long Island Sound. *Estuaries* 24, 228–243. doi: 10.2307/1352947

Aurin, D. A., Dierssen, H. M., Twardowski, M. S., and Roesler, C. S. (2010). Optical complexity in Long Island Sound and implications for coastal ocean color remote sensing. *JGR Oceans* 115, C7. doi: 10.1029/2009JC005837

Bricker, S. B., Longstaff, B., Dennison, W., Jones, A., Boicourt, K., Wicks, C., et al. (2008). Effects of nutrient enrichment in the nation's estuaries: A decade of change. *Harmful Algae* 8, 21–32. doi: 10.1016/j.hal.2008.08.028

Bukata, R. P., Jerome, J. H., Kondratyev, K. Y., and Pozdnyakov, D. V. (1995). *Optical properties and remote sensing of inland and coastal waters* (Boca Raton, FL: CRC Press).

Cao, F., and Tzortziou, M. (2024). Impacts of hydrology and extreme events on dissolved organic carbon dynamics in a heavily urbanized estuary and its major tributaries: a view from space. *JGR Biosci.* 129. doi: 10.1029/2023JG007767

Cao, Z., Wang, M., Ma, R., Zhang, Y., Duan, H., Jiang, L., et al. (2024). A decade-long chlorophyll-a data record in lakes across China from VIIRS observations. *Remote Sens. Environ.* 301, 113953. doi: 10.1016/j.rse.2023.113953

Ciotti, A. M., and Bricaud, A. (2006). Retrievals of a size parameter for phytoplankton and spectral light absorption by colored detrital matter from water-leaving radiances at SeaWiFS channels in a continental shelf region off Brazil. *Limnol. Oceanogr. Methods* 4, 237-253. doi: 10.4319/lom.2006.4.237

El-Habashi, A., Ahmed, S., Ondrusek, M., and Lovko, V. (2019). Analyses of satellite ocean color retrievals show advantage of neural network approaches and algorithms that avoid deep blue bands. *J. Appl. Remote Sens.* 13, 024509. doi: 10.1117/1.JRS.13.024509

El-Habashi, A., Duran, C. M., Lovko, M., Tomlinson, M. C., Stumpf, R. P., and Ahmed, S. (2017). Satellite retrievals of Karenia brevis harmful algal blooms in the West Florida Shelf using neural networks and impacts of temporal variabilities. *J. Appl. Remote Sens.* 11, 032408. doi: 10.1117/1.JRS.11.032408

El-Habashi, A., Ioannis, I., Tomlinson, M. C., Stumpf, R. P., and Ahmed, S. (2016). Satellite retrievals of Karenia brevis harmful algal blooms in the West Florida Shelf using neural networks and comparisons with other techniques. *Remote Sens* 8, 377. doi: 10.3390/rs8050377

EUMETSAT (2021). *Sentinel-3 OLCI L2 report for baseline collection ol_l2m_003.* Available online at: https://www.eumetsat.int/media/47794 (Accessed December 20, 2022).

EUMETSAT (2022). *Recommendations for sentinel-3 OLCI ocean colour product validations in comparison with in situ measurements – matchup protocols.* Available online at: https://www.eumetsat.int/media/44087 (Accessed December 20, 2022).

Freitas, F., and Dierssen, H. M. (2019). Evaluating the seasonal and decadal performance of red band difference algorithms for chlorophyll in an optically complex estuary with winter and summer blooms. *Rem. Sens. Env.* 231, 11228. doi: 10.1016/j.rse.2019.111228

Gilerson, A. A., Gitelson, A. A., Zhou, J., Gurlin, D., Moses, W., Ioannou, I., et al. (2010). Algorithms for remote estimation of chlorophyll-a in coastal and inland waters using red and near infrared bands. *Optics Express* 18, 24109-24125. doi: 10.1364/OE.18.024109

Gilerson, A., Herrera-Estrella, E., Agagliate, J., Foster, R., Gossn, J. I., Dessailly, D., et al. (2023). Determining the primary sources of uncertainty in the retrieval of marine remote sensing reflectance from satellite ocean color sensors II. Sentinel 3 OLCI sensors. *Front. Remote Sens.* doi: 10.3389/frsen.2023.1146110

Gilerson, A., Herrera-Estrella, E., Foster, R., Agagliate, J., Hu, C., Ibrahim, A., et al. (2022). Determining the primary sources of uncertainty in retrieval of marine remote sensing reflectance from satellite ocean color sensors. *Front. Remote Sens.* doi: 10.3389/frsen.2022.857530

Gilerson, A., and Huot, Y. (2017). "Sun-induced chlorophyll-a fluorescence," in *Bio-optical modelling and remote sensing of inland waters* (Elsevier). doi: 10.1016/B978-0-12-804644-9.00007-0

Gilerson, A., Malinowski, M., Herrera, E., Tomlinson, M., Stumpf, R., and Ondrusek, M. (2021). "Estimation of chlorophyll-a concentration in complex coastal waters from satellite imagery," in *Proc. of SPIE 11752, Ocean Sensing and Monitoring XIII.* doi: 10.1117/12.2588004

Gilerson, A., Ondrusek, M., Tzortziou, M., Foster, R., El-Habashi, A., Tiwari, S. P., et al. (2015). Multi-band algorithms for the estimation of chlorophyll concentration in the Chesapeake Bay. *Proc. SPIE* 9638. doi: 10.1117/12.2195725

Gilerson, A., Zhou, J., Fortich, R., Ioannou, I., Hlaing, S., Gross, B., et al. (2007). "Spectral dependence of the bidirectional reflectance function in coastal waters and its impact on retrieval algorithms," in *Proc. of IEEE 2007 International Geoscience and Remote Sensing Simposium (IGARSS 2007)*, Barcelona, Spain.

Gitelson, A. A. (1992). The peak near 700 nm on radiance spectra of algae and water: relationships of its magnitude and position with chlorophyll concentration. *Int. J. Remote Sens.* 13, 3367-3373. doi: 10.1080/01431169208904125

Gitelson, A. A., Schalles, J. F., and Hladik, C. M. (2007).Remote chlorophyll-a retrieval in turbid, productive estuaries: Chesapeake Bay case study. *Rem. Sens. Env.* 109. doi: 10.1016/j.rse.2007.01.016

Gordon, H. R. (2005). Normalized water-leaving radiance: revisiting the influence of surface roughness. *Appl. Opt.* 44, 241–248. doi: 10.1364/AO.44.000241

Gower, J. F. R., Brown, L., and Borstad, G. A. (2004). Observation of chlorophyll fluorescence in west coast waters of Canada using the MODIS satellite sensor. *Can. J. Rem. Sens.* 30, 1725. doi: 10.5589/m03-048

Groetsch, P., Foster, R., and Gilerson, A. (2020). Exploring the limits for sky and sun glint correction of hyperspectral above-surface reflectance observations. *Appl. Optics* 59, 2942–2954. doi: 10.1364/AO.385853

Groetsch, P. M. M., Gege, P., Simis, S. G. H., Eleveld, M. A., and Peters, S. W. M. (2017). Validation of a spectral correction procedure for sun and sky reflections in above-water reflectance measurements. *Opt. Express* 25, A742–A761. doi: 10.1364/OE.25.00A742

Harding, L. W., Magnuson, A., and Mallonee, M. (2005). SeaWiFS retrievals of chlorophyll in Chesapeake Bay and the mid-Atlantic bight Estuarine. *Coast. Shelf Sci.* 62, 75–94. doi: 10.1016/j.ecss.2004.08.011

Harmel, T., Gilerson, A., Hlaing, S., Tonizzo, A., Legbandt, T., Weidemann, A., et al. (2011). Long island sound coastal observatory: assessment of above-water reflectance measurement uncertainties using collocated multi and hyper-spectral radiometers. *Appl. Optics* 50, 5842–5860. doi: 10.1364/AO.50.005842

Hieronymi, M., Müller, D., and Doerffer, R. (2017). The OLCI neural network swarm (ONNS): A bio-geo-optical algorithm for open ocean and coastal waters. *Front. Mar. Sci.* 4. doi: 10.3389/fmars.2017.00140

Hlaing, S., Harmel, T., Gilerson, A., Foster, R., El-Habashi, A., Bastani, K., et al. (2013). Evaluation of the VIIRS ocean color monitoring performance in coastal regions. *Remote Sens. Environ.* 139, 398–414. doi: 10.1016/j.rse.2013.08.013

Ioannou, I., Gilerson, A., Ondrusek, M., Foster, R., El-Habashi, A., et al. (2014). Algorithms for the remote estimation of chlorophyll-a in Chesapeake Bay. *Proc. SPIE*, 9111. doi: 10.1117/12.2053753

IOCCG (2006). "Remote sensing of inherent optical properties: fundamentals, tests of algorithms, and applications," in *Reports of the international ocean-color coordinating group, no. 5*. Ed. Z.-P. Lee(Dartmouth, Canada).

IOCCG (2010). "Atmospheric correction for remotely-sensed ocean-colour products," in *Reports of the international ocean-color coordinating group, no. 10, IOCCG*. Ed. M. Wang(Dartmouth, Canada). doi: 10.25607/OBP-101

IOCCG (2019). "Uncertainties in ocean colour remote sensing," in *Reports no. 18 of the international ocean-colour coordinating group*. Ed. F. Mélin (IOCCG, Dartmouth, NS). doi: 10.25607/OBP-696

IOCCG (2021). "Observation of harmful algal blooms with ocean colour radiometry," in *IOCCG report series, no. 20*. Eds. S. Bernard, R. Kudela, L. Robertson Lain and G. C. Pitcher (International Ocean Colour Coordinating Group, Dartmouth, Canada). doi: 10.25607/OBP-1042

Karlson, B., Andersen, P., Arneborg, L., Cembella, A., Eikrem, W., John, U., et al. (2021). Harmful algal blooms and their effects in coastal seas of Northern Europe. *Harmful Algae* 102, 101989. doi: 10.1016/j.hal.2021.101989

Le, C., Hu, C., Cannizzaro, J., English, D., and Muller-Karger, F. E. (2013). Evaluation of chlorophyll-A remote sensing algorithms for an optically complex estuary. *Remote Sens. Environ.* 129, 75-89. doi: 10.1016/j.rse.2012.11.001

Lee, Z., Carder, K. L., and Arnone, R. (2002). Deriving inherent optical properties from water color: a multiband quasi-analytical algorithm for optically deep water. *Appl. Opt.* 41, 5755–5772. doi: 10.1364/AO.41.005755

Lee, Z. P., Lubac, B., Werdell, J., and Arnone, R. (2009). *An update of the quasi-analytical algorithm (QAA_v5)*. Available online at: www.ioccg.org/groups/Software_OCA/QAA_v5.pdf (Accessed October 1, 2024).

Liu, X., and Wang, M. (2022). Global daily gap-free ocean color products from multi-satellite measurements. *Int. J. Appl. Earth Oserv. Geoinf.* 108, 102714. doi: 10.1016/j.jag.2022.102714

Magnuson, A., Harding, L. W.Jr., Mallonee, M. E., and Adolf, J. E. (2004). Bio-optical model for Chesapeake Bay and the middle Atlantic bight," Estuarine. *Coast. Shelf Sci.* 61, 403–424. doi: 10.1016/j.ecss.2004.06.020

Malinowski, M., Herrera-Estrella, E., Foster, R., Agagliate, J., and Gilerson, A. (2024). Estimation of uncertainties in above-water radiometric measurements from hyperspectral and polarimetric imaging. *Ocean Sens. Monit. XVI* 13061, 1306103. doi: 10.1117/12.3014923

Menendez, A., and Tzortziou, M. (2024). Driving factors of colored dissolved organic matter dynamics across a complex urbanized estuary. *Sci. Total Environ.* 921, 171083. doi: 10.1016/j.scitotenv.2024.171083

Mikelsons, K., and Wang, M. (2019). Optimal satellite orbit configuration for global ocean color product coverage. *Opt. Express* 27, A445–A457. doi: 10.1364/OE.27.00A445

Mikelsons, K., Wang, M., Kwiatkowska, E., Jiang, L., Dessailly, D., and Gossn, J. I. (2022). Statistical evaluation of sentinel-3 OLCI ocean color data retrievals. *IEEE Trans. Geosci. Remote Sens.* 60, 4212119. doi: 10.1109/tgrs.2022.3226158

Mobley, C. D. (1994). *Light and water: radiative transfer in natural waters* (San Diego, CA: Academic Press).

Morel, A. (1974). Light and water: radiative transfer in natural waters. In: N. G. Jerlov and E. S. Nielsen (Eds.), *Optical aspects of oceanography*. New York: Academic Press, pp. 1-24.

Moses, W. J., Gitelson, A. A., Berdnikov, S., and Povazhnyy, V. (2009). Satellite estimation of chlorophyll-a concentration using the red and NIR bands of MERIS—The azov sea case study. *IEEE Geosci. Remote Sens. Lett.* 6, 845–849. doi: 10.1109/LGRS.2009.2026657

Nechad, B., Ruddick, K., and Park, Y. (2010). Calibration and validation of a generic multi-sensor algorithm for mapping of total suspended matter in turbid waters. *Remote Sens. Environ.* 114, 854–866. doi: 10.1016/j.rse.2009.11.022

Neil, C., Spyrakos, E., Hunter, P. D., and Tyler, A. N. (2020). Corrigendum to "A global approach for chlorophyll-a retrieval across optically complex inland waters based on optical water types. *Remote Sens. Environ.* 229, 159–178. doi: 10.1016/j.rse.2019.04.027

Ocean Optics Protocols for Satellite Ocean Color Sensor Validation. (2003). *Ocean optics protocols for satellite ocean color sensor validation*, NASA/TM-2003-21621. Volume 5. G. S. Fargion and J. L. Mueller (Eds.) Goddard Space Flight Space Center, Greenbelt, Maryland 20771

O'Reilly, J. E., Maritorena, S., Mitchell, B.G., Siegel, D.A., Carder, K.L., Garver, S.A., et al. (1998). Ocean color chlorophyll algorithms for SeaWiFS. *J. Geophys. Res.* 103, 24937-24953. doi: 10.1029/98JC02160

O'Reilly, J. E., and Werdell, P. J. (2019). Chlorophyll algorithms for ocean color sensors - OC4, OC5 & OC6. *Rem. Sens. Env.* 229, 32-47. doi: 10.1016/j.rse.2019.04.021

Pahlevan, N., Smith, B., Alikas, K., Anstee, J., Barboso, C., Binding, C., et al. (2022). Simultaneous retrieval of selected optical water quality indicators from Landsat-8, Sentinel-2, and Sentinel-3. *Rem. Sens. Env.* 270, 112860. doi: 10.1016/j.rse.2021.112860

Pahlevan, N., Smith, B., Schalles, J., Binding, C., Cao, Z., Ma, R., et al. (2020). Seamless retrievals of chlorophyll-a from Sentinel-2 (MSI) and Sentinel-3 (OLCI) in inland and coastal waters: A machine-learning approach. *Rem. Sens. Env.* 240, 111604. doi: 10.1016/j.rse.2019.111604

Pope, R., and Fry, E. (1997). Absorption spectrum (380-700 nm) of pure waters: II. Integrating cavity measurements. *Appl. Opt.* 36, 87108723. doi: 10.1364/AO.36.008710

Ransibrahmanakul, V., and Stumpf, R. P. (2006). Correcting ocean colour reflectance for absorbing aerosols. *Int. J. Remote Sens.* 27, 1759–1774. doi: 10.1080/01431160500380604

Roesler, C. S., and Boss, E. (2003). Spectral beam attenuation coefficient retrieved from ocean color inversion. *Geophys. Res. Lett.* 30, 1468. doi: 10.1029/2002GL016185

Schaeffer, B. A., Whitman, P., Vandermeulen, R., et al. (2023). Assessing potential of the Geostationary Littoral Imaging and Monitoring Radiometer (GLIMR) for water quality monitoring across the coastal United States. *Mar. pollut. Bull.* 196, 115558. doi: 10.1016/j.marpolbul.2023.115558

Seegers, B. N., Stumpf, R. P., Schaeffer, B. A., Loftin, K. A., and Werdell, P. J. (2018). Performance metrics for the assessment of satellite data products: an ocean color case study. *Opt. Express* 26, 7404–7422. doi: 10.1364/OE.26.007404

Sherman, J., Tzortziou, M., Turner, K. J., Goes, J., and Grunert, B. (2023). Chlorophyll dynamics from Sentinel-3 using an optimized algorithm for ecological monitoring in complex urban estuarine waters. *Intern. J. @ Appl. Earth Observ. Geoinform.* 118, 103223. doi: 10.1016/j.jag.2023.103223

Shi, W., and Wang, M. (2013). Tidal effects on ecosystem variability in the Chesapeake Bay from MODIS-Aqua. *Remote Sens. Environ.* 138, 65–76. doi: 10.1016/j.rse.2013.07.002

Smith, M. E., Robertson Lain, L., and Bernard, S. (2018). An optimized Chlorophyll a switching algorithm for MERIS and OLCI in phytoplankton-dominated waters. *Remote Sens. Environ.* 215, 217-227. doi: 10.1016/j.rse.2018.06.002

Steinmetz, F., Deschamps, P. Y., and Ramon, D. (2011). Atmospheric correction in presence of sun glint: Application to MERIS. *Opt. Express* 19, 9780–9800. doi: 10.1364/OE.19.009783

Stramski, D., Bricaud, A., and Morel, A. (2001). Modeling the inherent optical properties of the ocean based on the detailed composition of the planktonic community. *Appl. Opt.* 40, 29292945. doi: 10.1364/AO.40.002929

Stumpf, R. P., and Pennock, J. R. (1989). Calibration of a general optical equation for remote sensing of suspended sediments in a moderately turbid estuary. *J. Geophys. Res.* 94, 14363–14371. doi: 10.1029/JC094iC10p14363

Stumpf, R. P., and Tyler, M. A. (1988). Satellite detection of bloom and pigment distributions in estuaries. *Remote Sens. Environ.* 24, 385–404. doi: 10.1016/0034-4257(88)90014-4

Sydor, M., and Arnone, R. A. (1997). Effect of suspended particulate and dissolved organic matter on remote sensing of coastal and riverine waters. *Appl. Opt.* 36, 69056912. doi: 10.1364/AO.36.006905

Tango, P. J., and Batiuk, R. A. (2016). Chesapeake Bay recovery and factors affecting trends: Long-term monitoring, indicators, and insights. *Region. Stud. Mar. Sci.* 4, 12–20. doi: 10.1016/j.rsma.2015.11.010.2016

Turner, K. J., Tzortziou, M., Grunert, B. K., Goes, J., and Sherman, J. (2022). Optical classification of an urbanized estuary using hyperspectral remote sensing reflectance. *Optics Express* 30, 41590–41612. doi: 10.1364/OE.472765

Twardowski, M. S., Boss, E., Macdonald, J. B., Pegau, W. S., Barnard, A. H., and Zaneveld, J. V. (2001). A model for estimating bulk refractive index from the optical

backscattering ratio and the implications for understanding particle composition in case I and case II waters. *J. Geoph. Res.* 106, 1412914142. doi: 10.1029/2000JC000404

Tzortziou, M., Herman, J. R., Gallegos, C. L., Neale, P. J., Subramaniam, A., Harding, L. W. Jr., et al. (2006). Bio-optics of the Chesapeake Bay from measurements and radiative transfer closure. *Estuarine Coast. Shelf Sci.* 68, 348-362. doi: 10.1016/j.ecss.2006.02.016

Voss, K. J. (1992). A spectral model of the beam attenuation coefficient in the ocean and coastal areas. *Limnol. Oceanogr.* 37, 501509. doi: 10.4319/lo.1992.37.3.0501

Wang, M. (2006). Effects of ocean surface reflectance variation with solar elevation on normalized water-leaving radiance. *Appl. Opt.* 45, 4122–4128. doi: 10.1364/AO.45.004122

Wang, M., and Jiang, L. (2018). VIIRS-derived ocean color product using the imaging bands. *Remote Sens. Environ.* 206, 275–286. doi: 10.1016/j.rse.2017.12.042

Wang, M., Jiang, L., Son, S., Liu, X., and Voss, K. J. (2020). Deriving consistent ocean biological and biogeochemical products from multiple satellite ocean color sensors. *Opt. Express* 28, 2661–2682. doi: 10.1364/OE.376238

Wang, M., and Son, S. (2016). VIIRS-derived chlorophyll-a using the ocean color index method. *Remote Sens. Environ.* 182, 141–149. doi: 10.1016/j.rse.2016.05.001

Werdell, P. J., and Bailey, S. W. (2005). An improved *in-situ* bio-optical data set for ocean color algorithm development and satellite data product validation. *Rem. Sens. Env.* 98, 122-140. doi: 10.1016/j.rse.2005.07.001

Werdell, P. J., Behrenfeld, M. J., Bontempi, P. S., Boss, E., Davis, E.T., Franz, B. A., et al. (2019). The Plankton, Aerosol, Cloud, ocean Ecosystem (PACE) mission: Status, science, advances," Bull. *Am. Meteorol. Soc* 100, 1775–1794. doi: 10.1175/BAMS-D-18-0056.1

Werther, M., Odermatt, D., Simis, S. G. H., Gurlin, D., Daniel, S. F., Jorge, D. S. F., et al. (2022). Characterizing retrieval uncertainty of chlorophyll-*a* algorithms in oligotrophic and mesotrophic lakes and reservoirs. *ISPRS J. Photogramm. Remote Sens.* 190, 279–300. doi: 10.1016/j.isprsjprs.2022.06.015

Windle, A. E., Evers-King, H., Loveday, B. R., Ondrusek, M., and Silsbe, G. M. (2022). Evaluating atmospheric correction algorithms applied to OLCI Sentinel-3 data of Chesapeake Bay Waters. *Remote Sens.* 14, 1881. doi: 10.3390/rs14081881

Wolny, J. L., Tomlinson, M. C., Schollaert Uz, S., Egerton, T. A., McKay, J. R., Meredith, A., et al. (2020). Current and future remote sensing of harmful algal blooms in the Chesapeake Bay to support the shellfish industry. *Front. Mar. Sci.* 7, 337. doi: 10.3389/fmars.2020.00337

Wynne, T. T., Meredith, A., Briggs, T., and Litaker, W. (2018). Harmful algal bloom forecasting branch ocean color satellite imagery processing guidelines. *NOAA Tech. Memo. NOS NCCOS* 252, 48. doi: 10.25923/twc0-f025

Wynne, T. T., Tomlinson, M. C., Briggs, T. O., Mishra, S., Meredith, A., Vogel, R. L., et al. (2022). Evaluating the efficacy of five chlorophyll-a algorithms in chesapeake bay (USA) for operational monitoring and assessment. *J. @ Mar. Sc. Eng.* 10, 1104. doi: 10.3390/jmse10081104

Zheng, G., Stramski, D., and DiGiacomo, P. M. (2015). A model for partitioning the light absorption coefficient of natural waters into phytoplankton, nonalgal particulate, and colored dissolved organic components: A case study for the Chesapeake Bay. *J. Geophys. Res. Oceans* 120, 2601–2621. doi: 10.1002/2014JC010604

Zibordi, G., Holben, B. N., Talone, M., D'Alimonte, D., Slutsker, I., Giles, D. M., et al. (2021). Advances in the ocean color component of the aerosol robotic network (AERONET-OC). *Ocean Technol.* 38, 725–746. doi: 10.1175/JTECH-D-20-0085.1

Zibordi, G., Kwiatkowska, E., Melin, F., Talone, M., Cazzaniga, I., Dessailly, D., et al. (2022). Assessment of OLCI-A and OLCI-B radiometric data products across European seas. *Remote. Sens. Environ.* 272, 112911. doi: 10.1016/j.rse.2022.112911

Zibordi, G., Mélin, F., Berthon, J. F., Holben, B., Slutsker, I., Giles, D., et al. (2009). AERONET-OC: A network for the validation of ocean color primary products. *J. Atmos. Ocean Technol.* 26, 1634–1651. doi: 10.1175/2009JTECHO654.1